Cell Reports

Article

Organotypic endothelial adhesion molecules are key for *Trypanosoma brucei* tropism and virulence

Graphical abstract

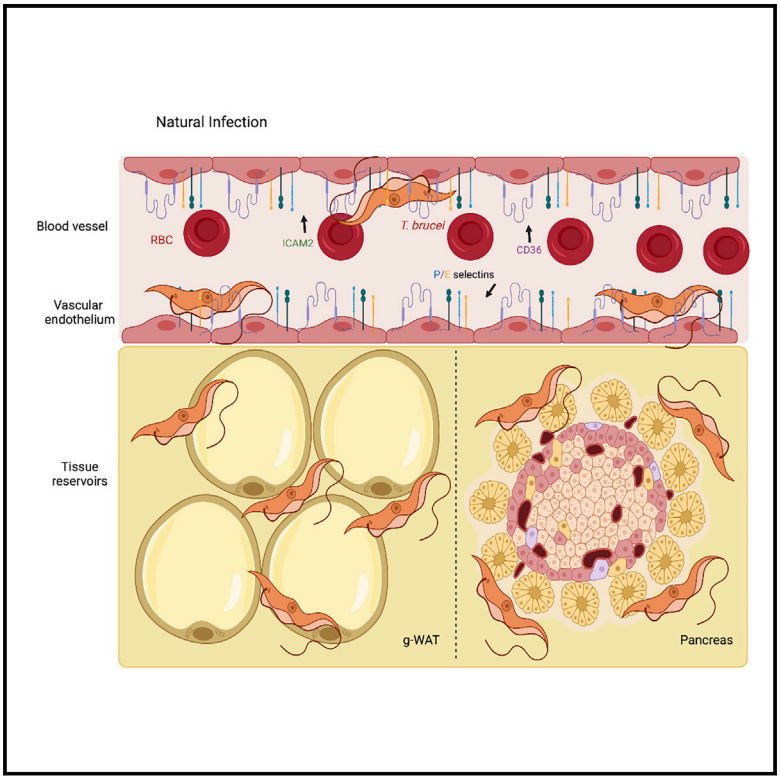

Authors

Mariana De Niz, Daniela Brás, Marie Ouarné, ..., Lenka Henao Misikova, Claudio A. Franco, Luisa M. Figueiredo

Correspondence

lmf@medicina.ulisboa.pt

In brief

Trypanosoma brucei are parasites that cause severe disease in mammals. De Niz et al. investigate how *T. brucei* interacts with blood vessels to preferentially traverse into certain organs, where they establish vast reservoirs. Selective removal of organ-specific vascular receptors ultimately alters parasite virulence and host survival.

Highlights

- Our study investigates the blood vasculature for *T. brucei* reservoir establishment
- We show the pancreas is a large extravascular reservoir
- We establish that *T. brucei* tropism is linked to organotypic adhesion molecules
- Interfering with adhesion molecules impacts parasite virulence and host survival

De Niz et al., 2021, Cell Reports *36*, 109741
September 21, 2021
https://doi.org/10.1016/j.celrep.2021.109741

CellPress

Cell Reports

CellPress
OPEN ACCESS

Article

Organotypic endothelial adhesion molecules are key for *Trypanosoma brucei* tropism and virulence

Mariana De Niz,[1,4] Daniela Brás,[1,5] Marie Ouarné,[1] Mafalda Pedro,[1,2] Ana M. Nascimento,[1,3] Lenka Henao Misikova,[1] Claudio A. Franco,[1,6] and Luisa M. Figueiredo[1,6,7,*]

[1]Instituto de Medicina Molecular Joao Lobo Antunes, Faculdade de Medicina, Universidade de Lisboa, Lisboa 1649-028, Portugal
[2]Departamento de Ciências da Vida, Faculdade de Ciências e Tecnologia, Universidade Nova de Lisboa, Caparica 2825-149, Portugal
[3]Bioimaging Unit, Instituto de Medicina Molecular Joao Lobo Antunes, Faculdade de Medicina, Universidade de Lisboa, Lisboa 1649-028, Portugal
[4]Present address: Institut Pasteur, Paris 75015, France
[5]Present address: Instituto Gulbenkian de Ciência, Oeiras 2780-156, Portugal
[6]Senior author
[7]Lead contact
*Correspondence: lmf@medicina.ulisboa.pt
https://doi.org/10.1016/j.celrep.2021.109741

SUMMARY

Trypanosoma brucei is responsible for lethal diseases in humans and cattle in Sub-Saharan Africa. These extracellular parasites extravasate from the blood circulation into several tissues. The importance of the vasculature in tissue tropism is poorly understood. Using intravital imaging and bioluminescence, we observe that gonadal white adipose tissue and pancreas are the two main parasite reservoirs. We show that reservoir establishment happens before vascular permeability is compromised, suggesting that extravasation is an active mechanism. Blocking endothelial surface adhesion molecules (E-selectin, P-selectins, or ICAM2) significantly reduces extravascular parasite density in all organs and delays host lethality. Remarkably, blocking CD36 has a specific effect on adipose tissue tropism that is sufficient to delay lethality, suggesting that establishment of the adipose tissue reservoir is necessary for parasite virulence. This work demonstrates the importance of the vasculature in a *T. brucei* infection and identifies organ-specific adhesion molecules as key players for tissue tropism.

INTRODUCTION

Tissue-specific tropism within vertebrate hosts has been the focus of great interest in the field of parasitology in recent years. However, the cellular and molecular adaptations that allow parasite tropism are still poorly understood. For many parasites, tropism to specific organs is an essential step of their life cycle, because the organs provide a niche for persistence, latency or dormancy, massive replication and/or growth, protection from the host immune responses, or differentiation into alternative stages essential for completion of the life cycle, among others (Boyett and Hsieh, 2014; Fernandes and Andrews, 2012; Guérin and Striepen, 2020; Lima and Lodoen, 2019; Onyilagha and Uzonna, 2019; Prudêncio et al., 2006; Rénia and Goh, 2016; Silva Pereira et al., 2019; Venugopal et al., 2020).

Trypanosoma brucei is a parasitic organism transmitted by tsetse flies (*Glossina* spp.), responsible for human African trypanosomiasis (HAT) in humans and nagana in other mammals. It requires two hosts to live and reproduce, namely, the insect vector and the mammalian host (Centers for Disease Control and Prevention, 2019). *T. brucei* invades the bloodstream and lymph and disseminates across the host body (Krüger and Engstler, 2018). The adipose tissue, skin, and brain have been identified as important extravascular reservoirs of *T. brucei* because of the numbers of parasites harbored, the role they play in parasite transmission, or the associated pathology, respectively (Casas-Sánchez and Acosta-Serrano, 2016; De Niz et al., 2019a–c; Silva Pereira et al., 2019). Yet, the relative contribution of parasite tissue reservoirs to overall parasitemia and disease outcome is unclear.

The relevance of the vascular endothelium for tropism and parasite dissemination has been studied in detail in the context of other parasites. For instance, *Plasmodium*-infected red blood cells (RBCs) undergo sequestration in the vasculature of several organs. Multiple endothelial cell (EC) receptors, including intercellular adhesion molecule 1 (ICAM1), endothelial protein C receptor (EPCR), platelet/endothelial cell adhesion molecule 1 (PECAM1), and CD36, have been associated with sequestration in specific tissues in both human and rodent malaria infections (Fonager et al., 2012; Hviid and Jensen, 2015; De Niz et al., 2016; Smith et al., 2001). While *Plasmodium* asexual blood stages are unable to cross the vascular endothelium, *T. brucei* extravasation has been studied in the brain. Two key findings include that a trypanosome-derived cathepsin L-like cysteine protease (brucipain) is required for traversal of the brain-blood barrier, and that vascular permeability does not correlate with parasite dissemination in the brain (reviewed in Kristensson et al., 2010).

Here, we used intravital imaging to study the role of blood vessels in the establishment of *T. brucei* tissue reservoirs *in vivo*. We have characterized the dynamics of host-parasite interactions with the vascular endothelium and its relationship to parasite tropism. We identified the pancreas as another reservoir for *T. brucei*, which, together with the gonadal white adipose tissue (g-WAT), constitutes the organs with highest parasite density. We showed that g-WAT and pancreatic tropism depend on several adhesion molecules expressed at the surface of ECs. We found that extravasation into the adipose tissue is specifically affected by the adhesion molecule CD36, and we demonstrated that the establishment of this reservoir is a key virulence mechanism with great impact in disease outcome. Our analysis shows that the vasculature plays an essential role in *T. brucei* infection, and that the establishment of tissue reservoirs increases the fitness of parasites and disease severity.

RESULTS

g-WAT tissue and pancreas are largest reservoirs of extravascular parasites

Little is known about the dynamics of *T. brucei* reservoir establishment *in vivo*. To evaluate parasite distribution in mice with high temporal resolution, we used a transgenic parasite line expressing the red-shifted firefly luciferase PpyREH9 and TdTomato fused with a TY1 tag (Calvo-Alvarez et al., 2018). We injected 2×10^3 parasites intraperitoneally in each mouse, and we followed the parasitemia *in vivo* in C57BL/6 and C57BL/6 Albino mice, the latter being a more suitable model to measure bioluminescence (Curtis et al., 2011; Doyle et al., 2004) (Figure S1A, left panel). In both mouse strains, we observed high blood parasitemia at days 5–8, and then later in infection, as previously reported (Calvo-Alvarez et al., 2018). Both strains of mice showed similar survival times, with 50% survival being reached by days 22–23 post-infection (Figure S1A, middle panel). Therefore, we limited the infection to day 20 for all subsequent experiments.

The relative whole-body bioluminescence measured in Albino mice (Figure 1A) correlated very well with blood parasitemia ($R^2 = 0.82$, $p < 0.001$) (Figure S1A, right panel). To determine relative parasite density in individual organs, we dissected each organ following injection of luciferin and performed *ex vivo* bioluminescence imaging (Figures 1B and 1C; Figure S1B). Three white and two brown adipose tissues (WATs and BATs, respectively) were collected (schematic shown in Figure S1C). Animals were not perfused prior to organ excision; therefore, the signal measured includes both intravascular and extravascular parasites (Figure 1C; Figure S1B). g-WAT, pancreas, and lungs (marked with arrows, Figure 1C) were the organs that presented the highest bioluminescence values throughout infection (Figure 1C; Figure S1B). For quantitative comparison, we show pooled bioluminescence values of all organs during the first peak of parasitemia (days 5–8 post-infection) (Figure 1D). The lungs, pancreas, and g-WAT showed around 30-fold higher bioluminescence than the average of other organs. Without perfusion, among adipose tissues, bioluminescence signal in the g-WAT was around 60- to 250-fold higher than other WAT depots ($p < 0.001$). Global comparisons between WAT and BAT depots showed that bioluminescence in BAT depots was significantly lower than WAT depots ($p = 0.04$) (Figure S1C). The pancreas was the organ with the highest accumulated daily intensity, being on average 2.8-fold higher than g-WAT and 22-fold higher than lungs considering the 20 days of infection. In the skin, we identified high heterogeneity in parasite distribution (Figure S1D), whereby some regions are highly enriched in parasites and others are not. This heterogeneity is consistent with previous observations (Capewell et al., 2016).

In the bloodstream, parasites are at very high concentrations (Figure S1A). To discriminate the bioluminescent signal between intravascular and extravascular compartments, we perfused mice prior to measuring bioluminescence to remove signal from intravascular parasites on day 6 post-infection (Figure 1E). In perfused mice, only g-WAT and pancreas showed significantly high bioluminescence. Upon perfusion, g-WAT was 200- to 4,800-fold higher than the four other WAT or BAT depots ($p < 0.001$ for all comparisons with g-WAT). At day 6 post-infection, the pancreas was equally enriched as the g-WAT ($p = 0.25$) and 1,000-fold higher than lungs ($p < 0.001$). Notably, the signal intensity in lungs decreased 200-fold after perfusion compared with non-perfused mice ($p < 0.001$) (Figures 1D and 1E), suggesting that most parasites in the lungs remained intravascular. These results were independent of the route of infection used (Figure S1E).

To confirm the bioluminescence results, we determined the intravascular and extravascular location of parasites in each organ at a single-cell level, using intravital microscopy (IVM) and *ex vivo* confocal microscopy (Figures 1F–1J; Video S1). Intravascular parasite density (parasites/10 mm^2) measured by intravital microscopy showed a similar pattern of parasite density in all organs, with two parasitemia ''waves'' in peripheral blood (Figure 1G), consistent with measurements performed by hemocytometer (Figure 1C; Figure S1A). Quantification of intravascular and extravascular parasites during the first parasitemia wave (days 5–8) (Figures 1I and IJ) confirmed a significant enrichment in the g-WAT and pancreas. Throughout infection, in total, the number of parasites per 10 mm^2 found in the extravascular space of g-WAT and pancreas corresponds to around 40% of the sum of extravascular parasites counted per 10 mm^2 in the 13 organs, while the three WAT depots together contribute to 48%.

The intravital imaging analysis identified four different patterns of intravascular and extravascular *T. brucei* distribution across organs (Figures 1G–1J; Figure S2). In group 1 (Figure S2A), there is proportionally more parasites in the extravascular space (blue) than intravascularly (red) throughout most of the infection. Group 2 (Figure S2B) has a pattern similar to group 1, in which the intravascular and extravascular compartments present two waves of parasite populations with a minimum around day 11, with the difference being that group 2 has consistently more intravascular than extravascular parasites. Given the consistency of patterns between the BAT and WAT groups, henceforth we use only one representative of each tissue category (gonadal for WAT and interscapular for BAT [i.e., isc-BAT]). In a third group (Figure S2C), the vast majority of parasites reside inside vessels, with a small population colonizing the extravascular space mostly after the first peak of blood parasitemia. Finally, the last group of organs (Figure S2D) showed an early

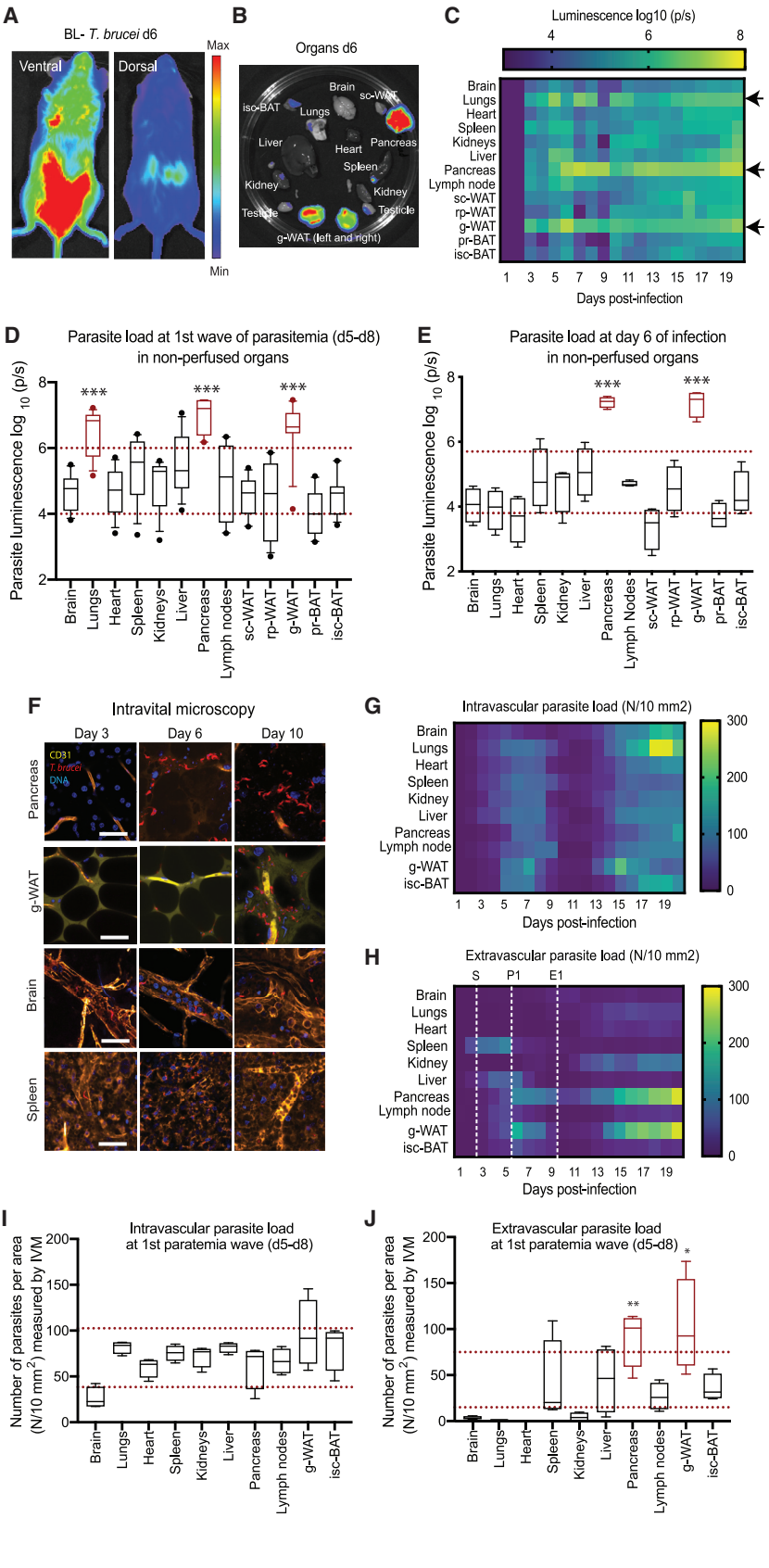

Figure 1. Identification of WAT and pancreas as the two main *T. brucei* extravascular reservoirs

(A) Representative images of whole-body bioluminescence in ventral (right panel) and dorsal (left panel) positions of a mouse infected with luciferase-expressing *T. brucei* at day 6 post-infection.

(B) Representative images of non-perfused organs collected from infected mice (day 6 post-infection).

(C) Mean bioluminescence (extravascular and intravascular parasites) values of individual mouse organs expressed as $\log_{10}$ light units per tissue area.

(D and E) Mean parasite density of individual organs during the first wave of parasitemia (days [d] 5–8) in non-perfused mice (D) and at day 6 post-infection in perfused mice (E) measured by bioluminescence ($\log_{10}$ light units per tissue area). All bioluminescence quantifications (A–D) correspond to values obtained from a minimum of nine mice.

(F) Immunofluorescence representative images obtained by intravital live imaging of parasites (TdTomato reporter, red) in g-WAT, pancreas, brain, and spleen at d3, d6 and d10 post-infection. Vessels are labeled with anti-CD31 antibody (yellow), interstitial space with FITC-Dextran, and nuclei with Hoechst (blue). Dyes and antibodies were administered by retroorbital intravenous injection 10–30 min prior to imaging. Scale bars, 50 μm.

(G and H) Heatmap of parasite density (number of parasites per tissue area) inside (G) or outside vessels (H). Dotted white lines denote the beginning of extravascular colonization (S [start], day 2), first peak of infection (P1, day 6), and the end of the first wave of parasitemia (E1 [end], day 10). For each day of infection, at least 100 fields of view were quantified, and the mean value is shown in the heatmap.

(I and J) Mean parasite density (number of parasites per tissue area) of individual organs inside (I) or outside (J) vessels during the first wave of parasitemia (d5–8), measured by intravital imaging.

For all relevant figures, dotted red lines show the interquartile range considering all organs. Organs above the upper threshold are considered significantly enriched, using an ANOVA statistical test. ***$p < 0.001$, **$p < 0.01$, *$p < 0.05$. All relevant data used to generate this figure are included in Data S1 (tabs 1–4). p/s, photons per second. See also Figures S1 and S2 and Videos S1 and S2.

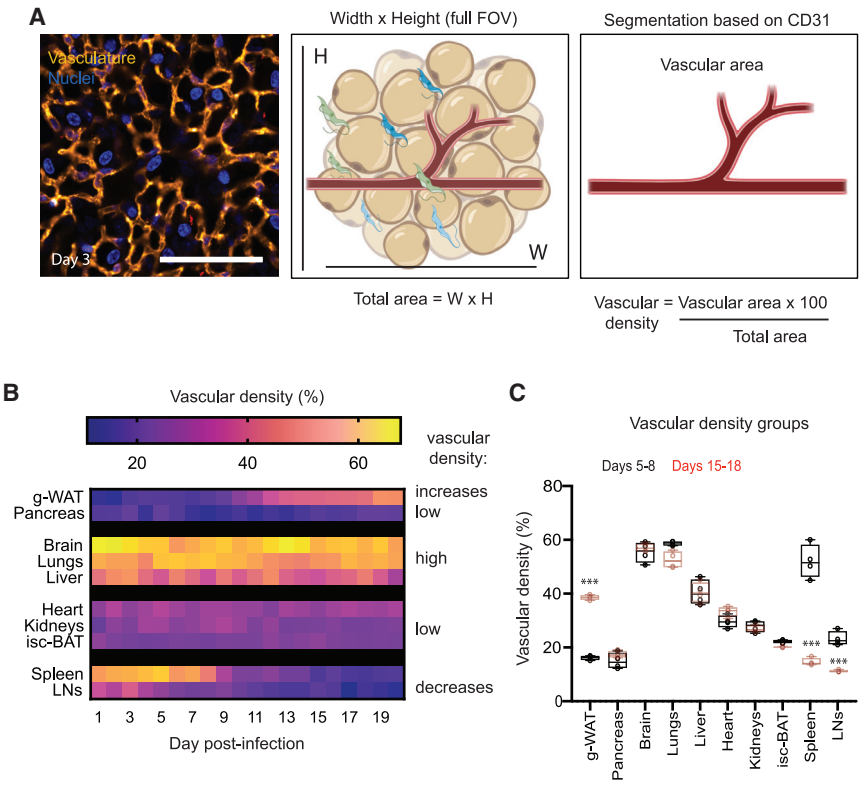

Figure 2. Changes in organ vascular density during *T. brucei* infection

(A) Vasculature is labeled with an antibody anti-CD31 (yellow), while nuclei are labeled by Hoechst (blue) upon retroorbital injection. Vascular density corresponds to the percentage of the imaged area filled with blood vessels based on the marker CD31 (middle and right panels). Scale bar, 50 μm.

(B) Heatmap of mean vascular density throughout 20 days of infection. At least 100 fields of view per day.

(C) Boxplot of mean vascular density for d5–8 (black) and d15–18 (red) depicted in (B).

For all graphs, significance is shown as ***p < 0.001, **p < 0.01, or *p < 0.05. All relevant data used to generate this figure are included in Data S1 (tabs 6 and 7). See also Figure S3.

extravascularization of parasites prior to the peak in the peripheral blood but little enrichment later in infection.

Altogether, these results indicate that parasite distribution in intravascular and extravascular spaces is very heterogenous across organs and varies with time. Importantly, in terms of establishment of an early tissue reservoir, we conclude that g-WAT and pancreas parasite reservoirs are established since day 3 post-infection, and that both remain the most parasitized organs throughout infection.

T. brucei enrichment in the pancreas and WATs is not correlated to vascular density

Next, we investigated the reasons for g-WAT and pancreatic tropism. First, we explored if there were differences in vascular density between organs. Vascular density indicates the percentage of the imaged area filled with blood vessels (marked by CD31/PECAM1, an EC receptor, or fluorescein isothiocyanate [FITC]-Dextran, a large polysaccharide that stays inside vessels unless there is increased vascular permeability) (Figure 2A).

In non-infected animals, we found that organs such as brain, lungs, liver, spleen, and lymph nodes are highly vascularized (30%–60% of their area consists of vessels), while adipose tissue depots, pancreas, heart, and kidneys are less vascularized (12%–30%) (Figures 2B and 2C; Figure S3), consistent with the literature (Cook, 1965). Figure 2C depicts vascular density during the first parasitemia wave (days 5–8, black boxes) and the last parasitemia wave (days 15–18, red boxes). During infection, vascular density remained unchanged in most organs, including pancreas. In contrast, vascular density in g-WAT significantly increased from 13% at day 1 to 49% at day 20 post-infection (Figure 2B; Figure S3), and it significantly decreased in spleen and lymph nodes from 51% and 36%, respectively at day 1 to 16% and 8%, respectively, at day 20 post-infection (Figure 2B; Figure S3). The increase in vascular density observed in the g-WAT coincides with and might be caused by tissue shrinkage by up to 82% probably because of extensive lipolysis during infection (also observed in other WATs) (Trindade et al., 2016). Conversely, the decrease in vascular density observed in the spleen and lymph nodes could be because of the dramatic tissue enlargement (increase of 60% and 210%) that these organs undergo as infection progresses.

When we compared the variation over time of the organ vascular density with the organ extravascular parasite density during 20 days of infection (Figure 1H), we found a significant correlation for some organs (g-WAT, pancreas, kidneys, isc-BAT, and spleen), but not others (heart, brain, lungs, liver, and lymph nodes). However, when we considered whether vascular density correlated with reservoir establishment (i.e., considering extravascular parasite density only the first 6 days of infection), we found only a significant correlation for the spleen (R^2 = 0.92, $p < 0.01$), whereas the g-WAT (R^2 = 0.13, $p = 0.54$) and pancreas (R^2 = 0.006, $p = 0.9$) showed no strong correlation. Altogether, we conclude that vascular density is not the reason why WAT and pancreas are the main reservoirs early in infection.

Parasite distribution across blood vessels is heterogeneous

Capillaries and post-capillary venules of several organs have been shown as important locations for *Plasmodium* sequestration (Franke-Fayard et al., 2010). Thus, we asked whether the type of vessel allowing parasite traversal is important for *T. brucei* tropism. In mammals, the vasculature is comprised of vessels of different diameters, of either arterial or venous origin (Figure 3A) (Betts et al., 2013; Tucker et al., 2020). We

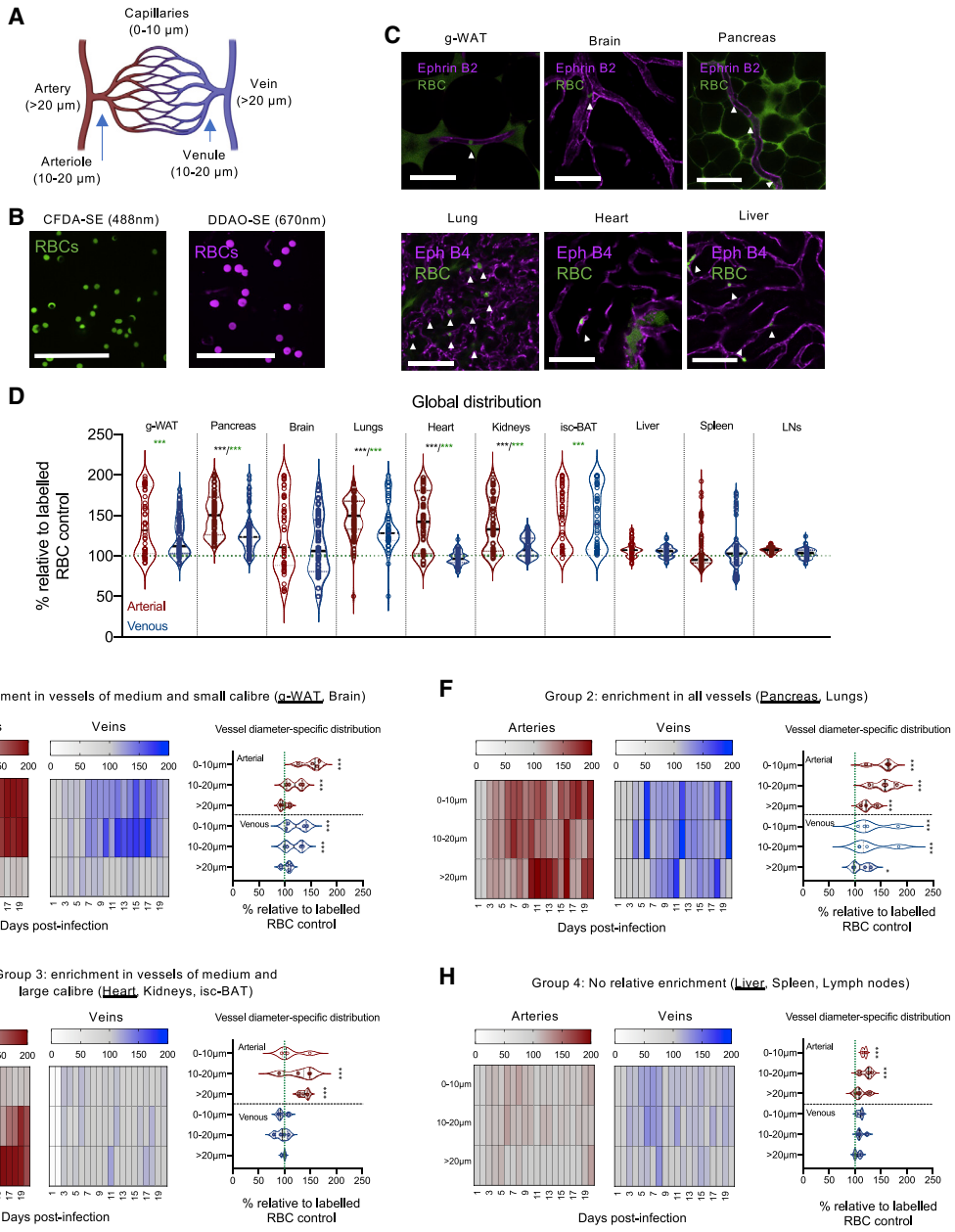

Figure 3. Distribution of *T. brucei* across arterial and venous vasculature is organ specific

(A) Schematic of arterial and venous vasculature, their deriving branches, and respective diameters.

(B) Representative microscopy images of carboxyfluorescein diacetate succinimidyl ester (CFDA-SE)- and 7-hydroxy-9H-(1,3-dichloro-9,9-dimethylacridin-2-one) succinimidyl ester (DDAO-SE)-labeled RBCs. Parasite concentration was calculated as the number of parasites relative to labeled RBCs. Scale bars, 20 µm.

(C) Representative immunofluorescence images show arteries as Ephrin B2-stained vessels, while veins are Ephrin B4-stained vessels. CFDA-SE-labeled RBCs are shown in green (marked by arrows). Scale bars, 50 µm.

(D) Violin plots of global parasite concentration relative to RBC in arterial or venous vasculature for the 10 organs analyzed in this study (green dotted line indicates that there are 100 parasites per 100 RBCs). Significance relative to RBC normalizers is shown as green asterisks.

(E–H) Heatmaps of parasite distribution in vasculature, relative to labeled RBCs. Panels are divided in arterial and venous vasculature. Violin plots of parasite concentration relative to RBC according to vessel diameter and vessel type. Data shown in the heatmaps and violon plots refer to the representative organ of each group, which is underlined.

For each day of infection, parasites were quantified in at least 100 fields of view. Significance is defined as follows: ***$p < 0.001$, **$p < 0.01$, or *$p < 0.05$. All relevant data used to generate this figure are included in Data S1 (tabs 8–9). See also Figures S4 and S5.

hypothesized that in the WAT and pancreas, parasites may accumulate in specific vessels, which could favor crossing from the blood into the extravascular space. To address this question, we injected uninfected and infected mice with exogenously labeled RBCs (as the basis for normalization for quantifications) and monitored their distribution across all vessel types, which were marked either with the pan-EC marker CD31, the arterial marker Ephrin B2, or the venous marker EphB4, conjugated to the Alexa 647 fluorophore (Figure 3B). It has been shown that the distribution of RBCs is proportional to the caliber and hemodynamics in each vessel (Carlson et al., 2008; Chien et al., 1966; Coppola and Caro, 2009; Secomb, 2016). For each day of the infection and for each organ, we surgically stopped blood flow and we quantified the number of parasites relative to the number of labeled RBCs. Vessels were classified according to their caliber either considering the total vasculature (Figure S4) or by venous and arterial identity (Figures 3E–3H). The longitudinal results of parasite concentration in each type of vessel are displayed as heatmaps, while the overall distribution for each condition is represented by violins plots (Figure 3; Figures S4 and S5).

Vessel caliber was the most important variable that contributed to heterogenous parasite distribution in the vasculature, when looking at total vasculature. We identified four phenotypes of parasite enrichment across organs (shown in Figure S4): group 1, enrichment in medium and small vessels (Figure S4B) in the brain and g-WAT; group 2, enrichment in all vessels (Figure S4C) in the pancreas and lungs; group 3, enrichment in medium and large vessels (Figure S4D) in the heart, kidneys, and isc-BAT; and group 4, no relative enrichment (Figure S4E) in the liver, spleen, and lymph nodes.

When taking into account arterial and venous identity, across the 20 days of infection, we saw that in g-WAT, parasite concentration is similar in arteries and veins ($p = 0.12$), as is the case also for the brain ($p = 0.16$), lungs ($p = 0.14$), isc-BAT ($p = 0.93$), liver ($p = 0.68$), spleen ($p = 0.74$), and lymph nodes ($p = 0.74$). In contrast, in pancreas ($p = 0.02$), heart ($p < 0.001$), and kidneys ($p = 0002$), parasites were globally more concentrated in arterial vessels (Figure 3D).

In g-WAT (Figure 3E), parasite concentration was highest in vessels of small and medium caliber of both arterial and venous identity, while in the brain the enrichment was mostly in arterial vasculature (Figure S5A). In the pancreas and lungs (Figure 3F; Figure S5B), parasites were highly enriched across arterial and venous vessels of all calibers. Although the heart, kidney, and isc-BAT (Figure 3G; Figure S5C) showed a higher parasite concentration in vessels of medium and large caliber, the heart mostly displayed enrichment in the arterial vasculature, while the kidneys and isc-BAT showed enrichment in both arterial and venous vasculature. Finally, in the spleen and lymph nodes (Figure S5D), parasite concentration was equivalent to the labeled RBC markers, showing no significant enrichment in any specific vessel type, while in the liver (Figure 3H), parasites seemed to be enriched in the arterial vasculature. Although parasite accumulation in small-diameter vessels of some organs can be explained by flow conditions characteristic of these organs, parasite enrichment in large vessels of the heart, kidneys, and isc-BAT was unexpected given the high flow characteristic of these vessels. This implies that parasites should exert significant forces to adhere to ECs.

In conclusion, our *in vivo* imaging demonstrates that the distribution of parasites across vessels is extremely heterogeneous, organ dependent, and time dependent. Our results are consistent with the notion that ECs have unique features in each organ, a concept termed organotypic vasculature (Augustin and Koh, 2017). However, organs with similar parasite distribution (i.e., g-WAT and brain, or the pancreas and lungs) do not form equivalent extravascular reservoirs. Thus, additional features should contribute to reservoir establishment.

Extravascular reservoirs are established before vascular permeability is compromised

Vascular permeability is typically increased during an infection and has previously been related to facilitating immune cell extravasation (Schnoor et al., 2015; Vestweber, 2015). Yet, changes in vascular permeability have not been previously studied in a *T. brucei* infection. We hypothesized that increases in vascular permeability could regulate parasite extravasation preferentially in the g-WAT and pancreas, allowing tissue tropism. To investigate vascular permeability, we intravenously injected mice with CD31 and 70 kDa FITC-Dextran and measured both the intravascular and extravascular mean fluorescence intensity (MFI) of FITC-Dextran using established methodology for intravital microscopy (Egawa et al., 2013). At basal conditions, albeit depending on each organ's inherent vascular permeability, most of the FITC-Dextran remains inside blood vessels. If the organ's vasculature becomes more permeable, FITC-Dextran will leak into the organ's parenchyma (Figure 4A).

The baseline extravascular MFI values in uninfected mice (controls) for FITC-Dextran depend on each organ's endogenous vascular permeability (Figure S6A). g-WAT and isc-BAT were the least permeable organs, followed by the brain, heart, and lungs. Spleen, pancreas, and lymph nodes showed intermediate levels of basal permeability, while the most permeable organs were the liver and kidneys (Figures S6B and S6C). Organ-specific permeability values in uninfected mice were used to calculate fold changes in permeability throughout infection (Figure 4).

Vascular permeability increased in all organs throughout infection (Figure 4B). However, we observed significant differences in the extent of such increase and in the day at which leakage was first detected (Figures 4B–4D; Figure S7). In g-WAT and pancreas, vasculature becomes more permeable from day 5 post-infection, followed by a progressive increase in permeability, and at the end of the infection (day 20), g-WAT is the tissue that shows the highest increase in permeability (14-fold). Figure 4B shows organs in increasing order of the onset of increased vascular permeability. Among these organs, the onset of increased vascular permeability happens on day 3 in spleen and lymph nodes, on day 5 in liver, kidney, and isc-BAT, on day 6 in brain and heart, and on day 7 in lungs. For most organs, maximum permeability is reached close to the end of the infection (day 20) (Figure 4B; Figure S7). Interestingly, in the brain, permeability remains low until day 7 and increases dramatically (2.6- to 5-fold, $p < 0.001$) on days 8–9, suggesting a significant disruption of the blood-brain barrier around this time. This is consistent with our IVM observations of petechiae and pools of

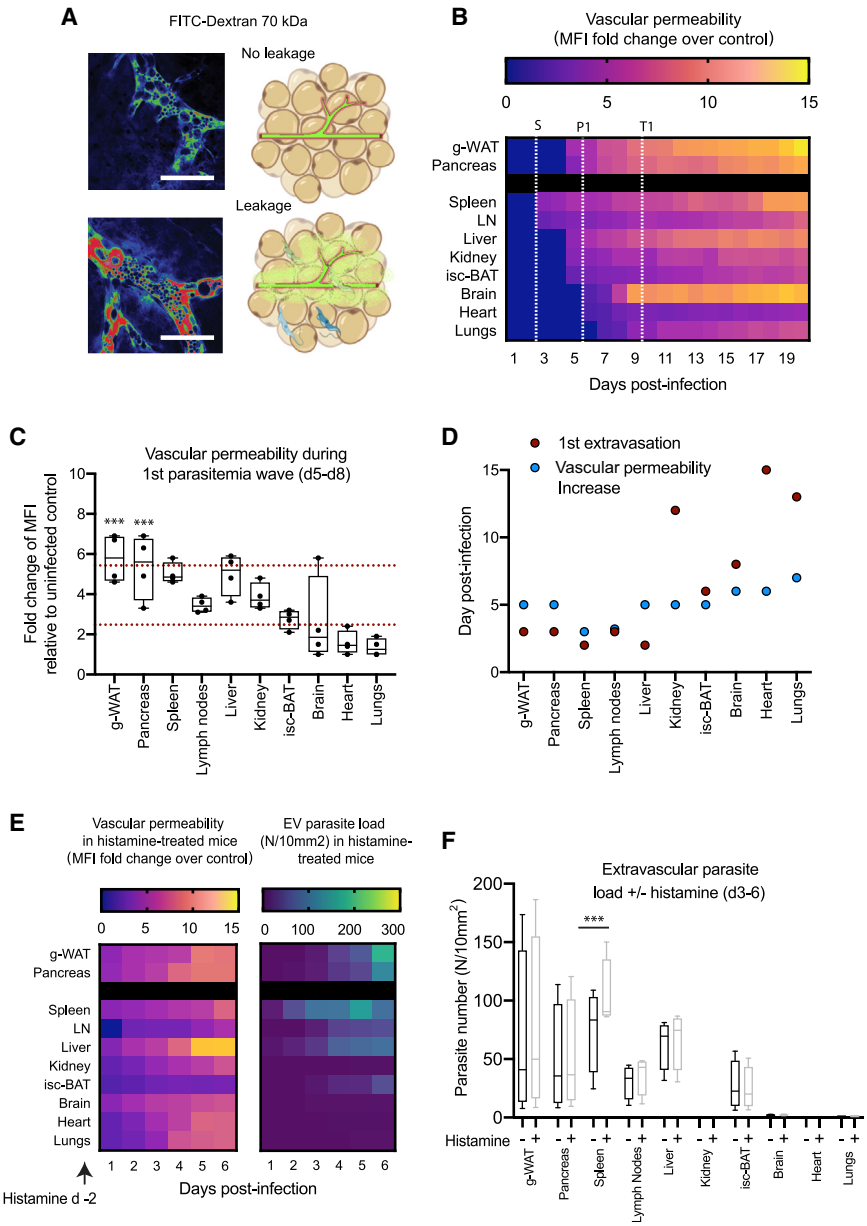

Figure 4. Changes in vascular permeability during *T. brucei* infection

(A) Vascular permeability was measured as an increase in the mean fluorescence intensity (MFI) emitted by the 70-kDa FITC-Dextran in the extravascular space per organ. Scale bar, 50 μm.

(B) Heatmap of vascular permeability every day of infection. Vascular permeability is calculated as the FITC-Dextran MFI in the extravascular space at each day post-infection relative to FITC-Dextran MFI in uninfected control (baseline values are shown in Figure S6). The white dotted lines show the infection events defined in Figure 1G.

(C) Boxplot showing quantitative values of vascular permeability corresponding to d5–8.

(D) Graphical representation comparing the time of increased *T. brucei* extravasation in each organ (red dot) and the time of increased vascular permeability (blue dot).

(E) Heatmaps of vascular permeability upon induction by histamine treatment 2 days prior to infection up to day 6 post-infection (left), an extravascular parasite density (right).

(F) Boxplots of extravascular parasite density at d3–6 post-infection in mice with (values from E, right panel) or without histamine treatment (values from Figure 1G).

For all graphs, significance is shown as ***$p < 0.001$, **$p < 0.01$, or *$p < 0.05$. For (B) and (H), FITC-Dextran was injected intravenously immediately prior to imaging, and at least 100 fields of view were used for measurements. Heatmap shows the mean of these values. All relevant data used to generate this figure are included in Data S1 (tabs 10–14). See also Figures S6 and S7.

FITC-Dextran across the brain from day 8 of infection onward (Figure S7).

When we compare the variation over time of the increase in vascular permeability of each organ with the extravascular parasite density, we found a significant correlation for most organs (R^2 values ranging between 0.2 and 0.83; p values ranging from 0.04 and <0.001), with the exception of the isc-BAT ($R^2 = 0.07$, $p = 0.24$) and lymph nodes ($R^2 = 0.07$, $p = 0.26$). g-WAT and pancreas showed significant correlations throughout the 20 days of infection ($R^2 = 0.42$, $p = 0.002$ for g-WAT; $R^2 = 0.64$, $p < 0.001$ for pancreas), and the highest fold change in the first parasitemia wave (Figure 4C). These results suggest that increased vascular permeability favors parasite extravasation in most organs. However, we noted that the sharp increase in parasite density in g-WAT and pancreas (at day 3 post-infection) precedes the increase in vascular permeability in these tissues (day 5 post-infection) (Figure 4D). Thus, parasites preferentially enter and accumulate in the extravascular spaces of g-WAT and pancreas before vascular integrity is compromised. Considering only days 1–5 of infection, we found no correlation between extravascular parasite density and vascular permeability in g-WAT and pancreas, suggesting that tissue tropism is independent of vascular permeability.

To further confirm that vascular leakage is not involved in the early colonization of g-WAT and pancreas, we induced vascular leakage with histamine, which induces vasodilation and increases leakiness (Egawa et al., 2013) (Figure 4E, left panel). Upon treatment of mice with histamine 2 days prior to infection with *T. brucei*, and during the first 3 days of infection, the 70-kDa FITC-Dextran presence in the organ's parenchyma revealed a generalized increased vascular permeability, leading to a 1.2- to 5-fold increase in permeability relative to untreated mice during the same days post-infection. We capped the analysis to day 6 post-infection, because this is the first time point by which the

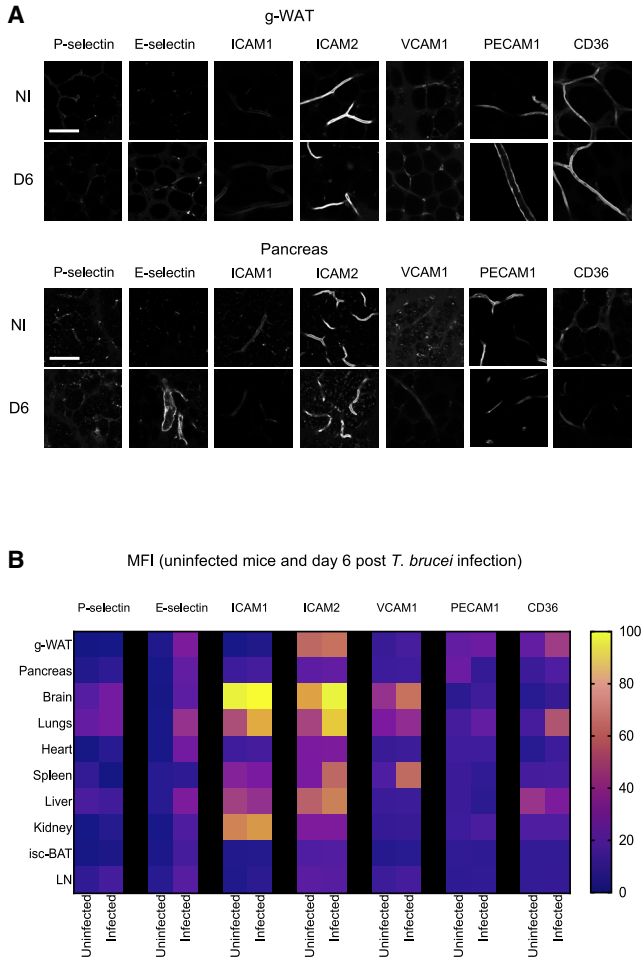

Figure 5. Changes in expression of vascular EC receptors during a *T. brucei* infection

(A) Expression of seven EC receptors (P-selectin, E-selectin, ICAM1, ICAM2, VCAM1, PECAM1, and CD36) measured by intravital imaging after injection of antibodies coupled to A647 fluorophore. Representative intravital images relative to g-WAT and pancreas. Scale bars: 50 μm.

(B) Heatmap shows MFI values for each receptor measured in each organ on uninfected and d6-infected mice. Measurements are the mean value of at least 100 vessels measured per condition.

All relevant data used to generate this figure are included in Data S1 (tabs 15 and 16). See also Figures S8 and S9 and Video S2.

tissue reservoirs are already established. In general, the treatment with histamine results in only a slight increase in the number of parasites in the parenchyma of most organs (with only the spleen showing a significant difference relative to untreated mice, $p < 0.01$) (Figure 4F). Importantly, the establishment of the tissue reservoirs in the g-WAT and pancreas does not start earlier than in non-treated conditions (Figure 4F).

Altogether we conclude that although vascular permeability is likely a key player for the presence of parasites in the extravascular space of various organs, it does not explain the initial establishment of the reservoirs in g-WAT and pancreas. These results suggest that the mechanism for tissue tropism is active and independent of vascular permeability.

Endothelial adhesion molecules are upregulated during infection

Our intravital imaging approach showed that parasites frequently contact ECs (Video S2). ECs are covered by many surface molecules that play important communication roles with circulating cells, including leukocytes or cancer cells (Muller, 2002, 2013; Vestweber, 2015; Wettschureck et al., 2019). Moreover, many of these adhesion molecules play a role in host-parasite interactions (Smith et al., 2001). To investigate whether EC surface proteins are involved in parasite extravasation, we began by measuring the protein expression levels of seven EC adhesion molecules in all the organs of non-infected or infected mice. We measured P-selectin, E-selectin, ICAM1, ICAM2, VCAM1, PECAM1, and CD36 by injecting fluorescently labeled antibodies against those adhesion molecules in non-infected mice and animals at day 6 post-infection and by measuring the fluorescence intensities by intravital microscopy (Figure 5; Figure S8). The route of injection (retroorbital or caudal intravenous) did not result in differently labeled vasculature (Figure S9). The heatmap shows the intensity of antibody staining in animals infected for 6 days relative to non-infected animals (Figure 5B).

We observed that several adhesion molecules become more abundant during infection, but the extent of this effect was very variable among organs and among adhesion molecules. Of note, E-selectin is the adhesion molecule that is more upregulated during infection (11.3-fold increase on average [$p < 0.001$], ranging from 2.5 to 26.7 across organs). In the g-WAT of infected animals, CD36 and E-selectin were significantly upregulated during infection (1.9- and 10.6-fold; $p < 0.001$). In the pancreas, E-selectin showed the highest upregulation following infection (13.6-fold, $p < 0.001$), while P-selectin (1.8-fold, $p < 0.001$) and CD36 (1.7-fold, $p < 0.001$) upregulation were also significant.

We conclude that during a *T. brucei* infection there are significant changes in the pattern of expression of the selected EC adhesion molecules, which indicates organ-specific molecular alterations in the vasculature during infection.

Adhesive molecules modulate *T. brucei* tissue colonization

Next, we investigated the effects of blocking each of these adhesion molecules on parasitemia and mouse survival. In addition, we targeted P-selectin in combination with E-selectin, because compensation mechanisms for both molecules have been reported (Hickey et al., 1999). We treated mice with the respective blocking antibodies for 8 days (from 2 days prior to infection until 6 days post-infection). We monitored peripheral parasitemia (Figures 6A and 6B). In general, when the effect of blocking a receptor led to a significant reduction in parasitemia in peripheral blood, it also led to an increase in mouse survival (Figure 6C). We observed that blocking E-selectin, P-selectin, ICAM2, CD36, and PECAM1 allowed 50% of animals to survive past day 40. Interestingly, simultaneous blocking of P- and E-selectin appears to have cured animals because no animals died (Figure 6C). In contrast, blocking ICAM1 and VCAM1 did not change parasitemia and resulted in a mixed survival phenotype (with some mice dying at similar times as control mice, while others had extended survival at around 10 days compared with controls).

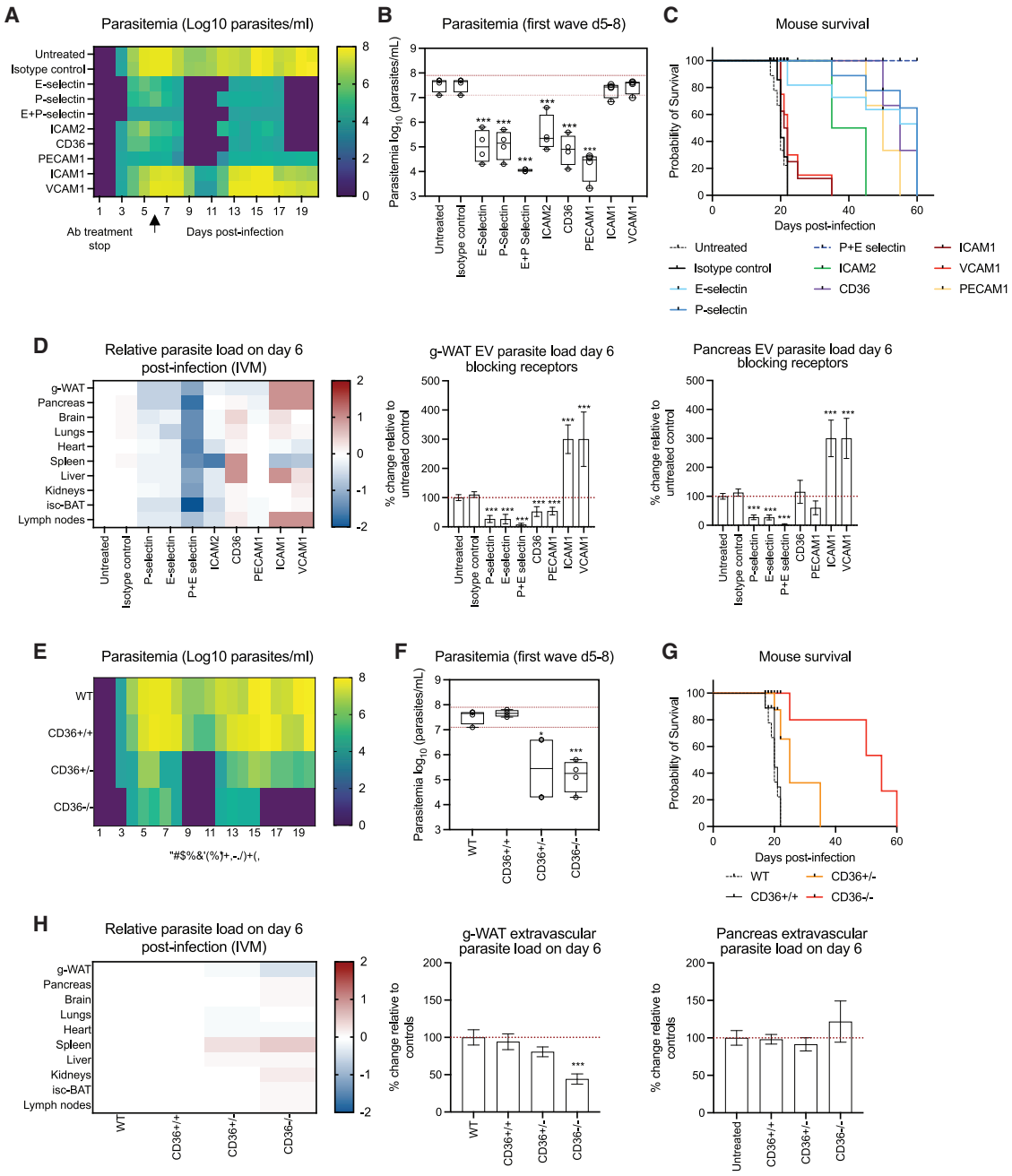

Figure 6. Blocking specific vascular EC receptors reduced *T. brucei* virulence and extravasation

(A) Parasitemia was followed by bioluminescence in mice treated with blocking antibodies 2 days prior to and during the initial 6 days of infection.

(B) Boxplots of mean parasitemia during the first parasite peak (d5–8).

(C) Survival of antibody-treated mice. ECl receptors recognized by antibodies are indicated in the key.

(D) Heatmap of parasite enrichment in multiple organs on d6 post-infection, calculated from the percentage of detected parasites per area in the extravascular space, in treated versus untreated conditions. Zero was set as the baseline control, and data are plotted in a log10 scale. Each column represents a different antibody treatment of infected mice. Graphs in the middle and right panels show the respective quantitative values of parasite density in g-WAT and pancreas. All other organs are included in Figure S10. Error bars show SD.

(E) Parasitemia was followed by hemocytometer in mice homozygous ($CD36^{-/-}$), heterozygous ($CD36^{+/-}$), or wild-type ($CD36^{+/+}$) for CD36 and mice treated with blocking antibodies 2 days prior to and during the initial 6 days of infection.

(F) Boxplots of the mean parasitemia during the first peak (d5–8).

(G) Mouse survival as assessed in genetically modified mice.

(legend continued on next page)

We then tested the role of these adhesion molecules in parasite extravasation and reservoir establishment. At day 6 post-infection (day 8 post-treatment), animals were subjected to intravital microscopy. Extravascular parasite density was measured by IVM, and data are presented in a heatmap as a fold change relative to (day 0) control (left panel) and as the percentage of values of WT untreated mice (whose value for each organ is taken as baseline, 100%) (Figure 6D; Figure S10). Interestingly, blocking ICAM1 and VCAM1 resulted in either no change or an increase in parasite density in most organs (except the spleen, where parasite density decreased significantly), while not affecting significantly overall blood parasitemia or mouse survival. Conversely, blocking PECAM1 had no effect on the presence of extravascular parasites in most organs (Figure 6D). The exceptions were the g-WAT and pancreas, where we observed a 2-fold decrease in extravascular parasite density ($p < 0.001$ and $p < 0.05$, respectively) (Figure 6D). A more pronounced effect was found upon blocking P- and E-selectin, which resulted in a ~2-fold decrease in parasite density ($p < 0.001$) in most organs and ~4-fold decrease ($p < 0.001$) for g-WAT and pancreas; a simultaneous block of both receptors resulted in a synergistic effect with an average drop in parasite density in all organs of ~20-fold ($p < 0.001$), including g-WAT and pancreas (Figure 6D).

CD36 is the most abundant g-WAT adhesion molecule, and its blocking resulted in g-WAT-specific phenotype. Although parasite density in the blood decreased 250-fold (Figures 6A and 6B), it led to a decrease of 2-fold ($p < 0.001$) in parasite density in the extravascular space of g-WAT, no change in pancreas, and a 1.5- to 3-fold ($p < 0.01$) increase in all other organs, including lung and liver, where CD36 is also highly expressed (Figures 5B and 6D). Consistent with an overall reduction in parasite burden, mice showed delayed lethality (Figure 6C). To further confirm that CD36 has a specific role on adipose tissue tropism, we infected mice in which one or both CD36 alleles were ablated ($CD36^{+/-}$ and $CD36^{-/-}$), and we followed parasitemia (Figures 6E and 6F), mouse survival (Figure 6G), and establishment of tissue reservoirs (Figure 6H). Homozygous knockout mice revealed exactly the same results as anti-CD36 blocking experiments: (1) reduced parasite density in adipose tissue and blood, but not in any other solid tissue; and (2) decreased mouse lethality. Interestingly, these phenotypes can already be detected with heterozygous mice, highlighting the importance of CD36 for *T. brucei* infection.

Overall, these data show that E- and P-selectins, ICAM2 and PECAM1, are necessary for parasite extravasation in most organs. Blocking these EC adhesion molecules resulted in a dramatic loss of fitness for the parasite population, as observed by a reduction in parasitemia and a corresponding reduction in disease burden and mortality for the host. Importantly, CD36 is specifically required for parasite extravasation in the g-WAT, but not in other organs, suggesting that adipose tissue tropism could be mediated by parasite interactions with CD36 at the surface of ECs in adipose tissue vessels.

CD36 facilitates interaction of parasites with ECs *in vitro*

To better understand the role of CD36 in the interactions between parasite and the vasculature, next we used *in vitro* assays. First, we asked whether parasites interacted with CD36 immobilized onto a plastic surface using an *in vitro* assay previously described (Figure 7A) (De Niz et al., 2016). Half a million *T. brucei* bloodstream form parasites were incubated for 1 h in Petri dishes previously coated with different concentrations of CD36 (Figure 7B). After washing, the proportion of parasites that remained attached to the surface was scored by microscopy. We found that up until 50 nM of CD36, only 1%–3% of parasites remained attached to the surface. However, when we used 100 nM or more of CD36, we observed that up to 12% of parasites attached ($p < 0.001$). Interestingly, up to 95% parasites attached to CD36 (but not to BSA), with the anterior side of the parasite, including the free flagellum and the parasite mid-body, suggesting that specific proteins located in this part of the parasite could mediate the interaction with CD36 (Figure 7C). Notably, parasites bound only by the flagellar tip were washed out in all experiments.

To replicate more closely the environment that the parasite faces *in vivo*, we established a second *in vitro* assay using human umbilical vein ECs (HUVECs) (Figure 7D). We seeded *T. brucei* parasites on top of WT, GFP-expressing, or CD36-expressing HUVEC monolayers for different periods of time and measured the number of parasites attached after washouts at each time point. In WT and control GFP-expressing HUVECs, we observed a baseline attachment of 15% of parasites following 30 min of incubation. Differences in attachment across the six time points measured were not significant in WT and GFP ($p = 0.56$ and $p = 0.71$, respectively). In CD36-expressing cells, a baseline attachment of 15% was also observed. However, percentages of attached parasites increased to 21% at 2–4 h and to 28% at 6–8 h. At 6–8 h, the differences relative to the control conditions (WT and GFP) were significant ($p = 0.01$) (Figure 7E). As observed in the assays using recombinant CD36, in EC-based assays, parasites preferentially attached to the host cells with the anterior side of the parasite, while attachment with only the flagellar tip resulted in removal upon washouts (Figure 7F).

Finally, we investigated whether the expression of CD36 at the surface of ECs influenced parasite extravasation. We established transwell migration assays, whereby we cultured a monolayer of WT, GFP-expressing, or CD36-expressing HUVECs on the base of the top chamber (Figure 7G). On the bottom compartment, we added HMI-11 media. We then added *T. brucei* parasites to the top chamber, and after 1-h incubation, we counted how many parasites crossed from the top to the

(H) Heatmap of parasite enrichment in multiple organs on day 6 post-infection, calculated from the ratio of detected parasites per area in the extravascular space, in mice homozygous or heterozygous for CD36 depletion versus wild-type littermates. Zero was set as the baseline control, and data are plotted in a log10 scale. Graphs in the middle and right panels show the extravascular parasite density in g-WAT and pancreas on day 6 post-infection.

For all experiments, measurements correspond to triplicate experiments obtained from 9–12 mice. Heatmaps correspond to the score of at least 100 measurements from at least 12 individual mice. Significance relative to untreated controls is shown as ***$p < 0.001$, **$p < 0.01$, or *$p < 0.05$. Error bars show SD. All relevant data used to generate this figure are included in Data S1 (tabs 17–20). See also Figures S10 and S11.

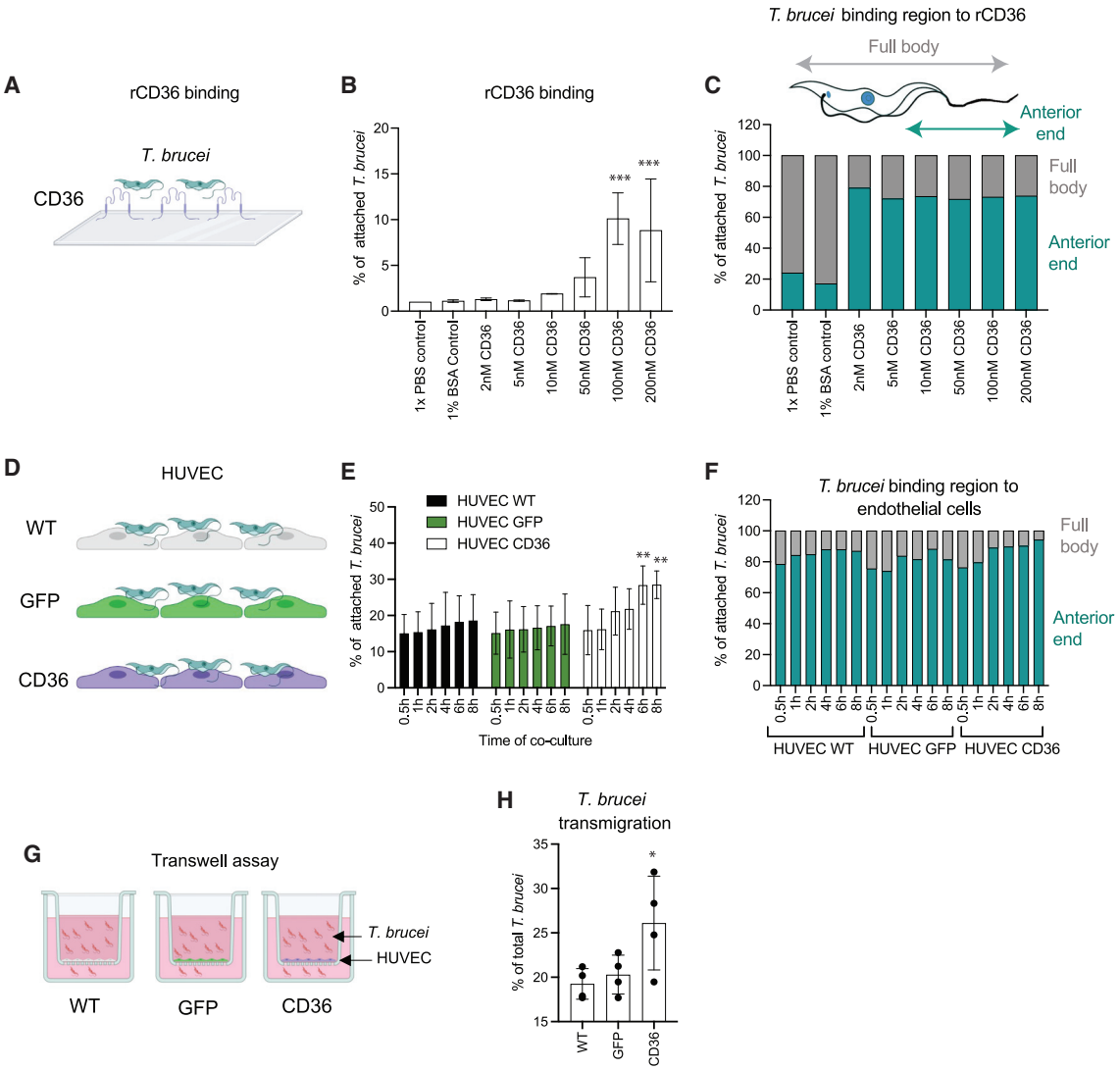

Figure 7. CD36 facilitates *T. brucei* binding to and transmigration through the vascular endothelium

(A) Schematic representation of static binding assay of *T. brucei* on plastic surfaces coated with recombinant mouse CD36 (rCD36).

(B) Proportion of parasites attached to plastic surface, coated with various concentrations of recombinant mouse CD36 (rCD36). 1× PBS and 1% BSA were used as binding controls.

(C) Parasite subcellular regions that bind to plastic surface. Following washouts, the proportion of parasites bound to plastic surface using the full body or the anterior end (which includes the mid-body and the free flagellum) were quantified.

(D) Schematic representation of static binding assay of *T. brucei* on WT HUVEC and HUVECs expressing GFP or CD36.

(E) Proportion of parasites attached to HUVECs (WT, GFP-, or CD36-expressing cells). Parasite attachment was quantified at six different time points (0.5, 1, 2, 4, 6, and 8 h). A statistical model considering time was performed.

(F) Parasite subcellular regions that bind to HUVECs. Quantification was as described in (C).

(G) Schematic representation of transwell assay of *T. brucei* on WT HUVEC and HUVECs expressing GFP or CD36. *T. brucei* were seeded on the top chamber for 1 h.

(H) Proportion of parasites that migrated from the top to bottom chambers of the transwell assay (Boyden chamber). EC barrier consisted of WT HUVEC cells and HUVEC cells expressing GFP or CD36.

For all panels, ANOVA tests were performed to determine significance. Significance is shown as ***$p < 0.001$, **$p < 0.01$, or *$p < 0.05$. Experiments were performed in triplicate, and 100 fields of view were quantified. Error bars show SD. All relevant data used to generate this figure are included in Data S1 (tabs 21–23).

bottom chamber. We found that in the presence of WT or GFP-expressing ECs, an average of 20% of parasites transmigrate. In CD36-expressing HUVECs, it increases up to 27% ($p = 0.03$ compared with WT) (Figure 7H).

Overall, we conclude that *T. brucei* interacts directly with CD36, and this interaction may facilitate the crossing of the EC barrier that separates the blood from the adipose tissue parenchyma.

DISCUSSION

T. brucei parasites are capable of crossing physical barriers separating tissues and the vascular system. By studying the interface between *T. brucei* and the blood vasculature in different organs *in vivo*, we discovered that crossing the vasculature and colonization of solid tissues is necessary for *T. brucei* virulence and greatly affects the disease outcome.

Parasite reservoirs and pathology

Using a combination of bioluminescence and IVM, we confirmed that the g-WAT is a major parasite reservoir (Trindade et al., 2016), and we identified a previously unknown reservoir: the pancreas. Previous works on *T. cruzi* (Corbett et al., 2002; Dufurrena et al., 2017; Martello et al., 2013), *Plasmodium* (Abhilash et al., 2016; Glaharn et al., 2018), and *Toxoplasma* (Nassief Beshay et al., 2018) have reported sequestration in pancreatic blood vessels, pancreatic invasion, and morphological changes in the pancreas, including acute pancreatitis in humans. The fact that the pancreas represents one of the largest reservoirs of an extracellular parasite, such as *T. brucei*, is puzzling, because the majority of the organ consists of exocrine tissue that produces pancreatic enzymes for digestion, including trypsin and chymotrypsin, amylase, and lipase (Shi and Liu, 2014). Why such environment is favorable for parasite survival and/or proliferation is unclear.

Comparative analysis of parasite density in several adipose tissue depots showed that although the g-WAT is the largest reservoir, overall WATs were significantly enriched in parasites compared with BATs. BAT and WAT are significantly different in their transcriptional, secretory, morphological, and metabolic signatures, and they play different roles (Hull and Segall, 1966; Rosell et al., 2014; Saely et al., 2012). We hypothesize that the BAT and WAT present different metabolites to the parasites, the latter of which favor the parasite reservoir. Moreover, in this work, we show that during a *T. brucei* infection, the WAT and BAT depots respond very different in almost all the features we assessed. The extent of the translational relevance of our findings on *T. brucei* tropism in WAT to humans and other natural hosts remains relatively unexplored. On this point, several comparative studies have highlighted similarities and differences between human and rodent models in terms of adipose tissue distribution, morphology, and adipokine functions (Zhang et al., 2018; Bowles and Kopelman, 2001). Nevertheless, WAT tropism could be an attractive target to explore in future clinical studies.

Another surprising finding was the highly heterogeneous patterns of parasite distribution in each organ over the course of infection. The heart, brain, lungs, and kidneys seemed to show high parasite extravasation late in infection and correlated with vascular permeability. Interestingly, these four organs have been associated with specific complications of *T. brucei* infection in humans. Conversely, another group of organs (liver, spleen, and lymph nodes) showed high extravascular enrichment early in infection. These organs are known to filter blood and/or are secondary lymphoid organs where immune responses can be initiated and maintained. Research in various pathogens has shown that early interactions with these organs ultimately lead to pathology. Such pathology may involve organ enlargement and remodeling, including the loss of specific areas necessary for the generation of adequate immune responses (Cadman et al., 2008; Engwerda et al., 2005; Magez et al., 2020; Martin-Jaular et al., 2011; Oster et al., 1980; Urban et al., 2005). In our work, we observed that this early invasion resulted in very high vascular permeability in the liver and significant enlargement of the spleen and lymph nodes. Altogether, at terminal points of infection, vascular pathology as assessed by leakiness is severe in most organs. Although a single cause of death is difficult to pinpoint, the various rodents analyzed show severe pathology in multiple organs, and it is possible that death might be because of multi-organ failure.

Importance of vasculature in parasite virulence

Observation of *T. brucei* interactions with blood vessels of the pancreas and WAT led us to hypothesize that parasites could interact with adhesion molecules at the surface of ECs, favoring transmigration. Blocking three different surface adhesion molecules in the first week of infection (E- and P- selectin, ICAM2, and PECAM1) resulted in a global reduction of parasite density in the blood and solid tissues, suggesting that parasites could become more vulnerable to the immune system when interaction with vasculature is blocked. Given the role of these receptors in leukocyte migration, we cannot exclude that blocking antibodies might affect leukocyte function, which could result in a stronger immune response in the blood. Importantly, the consequence of the 8-day antibody treatment was that animals survived much longer, and some even appear to have been cured. These results suggest that the parasite-vasculature interaction is a determinant for parasite virulence.

Although treatment against E- and P-selectin and ICAM2 had a global effect on parasite traversal, blocking CD36 (or genetically ablating it) resulted in reduced extravascular *T. brucei* density in the g-WAT. This suggests that CD36 specifically favors parasite extravasation in adipose tissue. The *in vitro* assays confirmed that *T. brucei* interacts with CD36 and also CD36 parasite transmigration through EC monolayers. We hypothesize that CD36 favors extravasation in WAT. In CD36-blocking experiments, the spleen, liver, and lymph nodes were highly parasitized, suggesting these organs could play a role in eliminating parasites that could not extravasate. Abrogation of CD36-mediated sequestration of *Plasmodium*-infected hosts also results in increased parasite density in the spleen, because they are more readily eliminated by this lymphoid organ (Fonager et al., 2012; De Niz et al., 2016).

Taken together, we propose a model for adipose tissue tropism whereby *T. brucei* frequently engages with EC surface proteins as parasites travel in the vasculature. Such interactions can be mediated by several adhesion molecules (CD36, ICAM2, E- and P-selectins). In the vasculature of the g-WAT, in addition to ICAM2, PECAM1, E-selectin, and P-selectin, the high expression of CD36 facilitates stronger interactions with *T. brucei*, which may direct or slow down parasites toward a putative crossing site, thus favoring extravasation. When adhesion molecules are blocked, *T. brucei* interactions with ECs are reduced, interfering with the normal extravasation of parasites. This results in more parasites being eliminated from the circulation

either by systemic immune responses and/or by the spleen. Remarkably, we unequivocally showed that interfering with host vasculature reduced pathology and mortality. Thus, pharmacological targeting of the parasite-EC interface may pave the way to the development of future therapies to tackle this medically relevant neglected tropical disease.

STAR★METHODS

Detailed methods are provided in the online version of this paper and include the following:

- KEY RESOURCES TABLE
- RESOURCE AVAILABILITY
  - Lead contact
  - Materials availability
  - Data and code availability
- EXPERIMENTAL MODEL AND SUBJECT DETAILS
  - Animals used
  - Trypanosoma brucei parasites and infections
  - HUVECs cell culture
  - HUVECs viral transduction
- METHOD DETAILS
  - Bioluminescence imaging (*in vivo* and *ex vivo*)
  - Intravital and *ex vivo* imaging
  - Intravascular and extravascular parasite quantification
  - Vascular density and diameter quantification
  - Vascular permeability quantification
  - Erythrocyte labeling and parasite quantification normalization by vascular type
  - Labeling endothelial receptors
  - Blocking endothelial receptors
  - Recombinant CD36 binding assays
  - CD36 binding assays in HUVECs
  - CD36 transmigration assays in HUVECs
- QUANTIFICATION AND STATISTICAL ANALYSIS

SUPPLEMENTAL INFORMATION

Supplemental information can be found online at https://doi.org/10.1016/j.celrep.2021.109741.

ACKNOWLEDGMENTS

The authors thank Brice Rotureau (Institut Pasteur) for providing the triple reporter (TY1-TdTomato-FLuc) AnTat1.1^{E} *T. brucei* parasite line. We thank Ruy M. Ribeiro for helpful advice for statistical analysis and Leonor Pinho for logistical help regarding experimental setups. We acknowledge the Rodent and Bioimaging Facilities of the Instituto de Medicina Molecular. We thank Maria Angeles Dominguez Cejudo from Claudio Franco's lab (IMM) for technical support. We also thank Francisca Vasconcelos, Sara Silva Pereira, Fabien Guegan, and Idalio Viegas for carefully reading this manuscript and providing helpful and critical feedback. This work was supported by HFSP (LT000047/2019-L) and EMBO (ALTF 1048-2016) to M.D.N. L.M.F. is an Investigator CEEC of the Fundação para a Ciência e a Tecnologia (CEECIND/03322/2108), and the laboratory is funded by ERC (FatTryp, ref. 771714). C.A.F. was supported by a European Research Council starting grant (679368), the Fondation Leducq (17CVD03), and the Fundação para a Ciência e a Tecnologia (grants IF/00412/2012, EXPL/BEX-BCM/2258/2013, PRECISE-LISBOA-01-0145-FEDER-016394, PTDC/MED-PAT/31639/2017, PTDC/BIA-CEL/32180/2017, and CEECIND/04251/2017).

AUTHOR CONTRIBUTIONS

Conceptualization, M.D.N., C.A.F., and L.M.F.; methodology, M.D.N., M.O., L.H.M., and A.M.N.; software, M.D.N.; validation, D.B. and M.P.; formal analysis, M.D.N., C.A.F., and L.M.F.; investigation, M.D.N., D.B., M.O., and M.P.; data curation, M.D.N.; writing – original draft, M.D.N., C.A.F., and L.M.F.; writing – review & editing, M.D.N., C.A.F., and L.M.F.; visualization, M.D.N., with significant input from C.A.F. and L.M.F.; supervision, C.A.F. and L.M.F.; project administration, M.D.N., C.A.F., and LM.F.; funding acquisition, M.D.N., C.A.F., and L.M.F.

DECLARATION OF INTERESTS

The authors declare no competing interests.

INCLUSION AND DIVERSITY

We worked to ensure diversity in experimental samples through the selection of the cell lines. One or more of the authors of this paper self-identifies as an underrepresented ethnic minority in science. While citing references scientifically relevant for this work, we also actively worked to promote gender balance in our reference list.

Received: April 2, 2021
Revised: June 29, 2021
Accepted: August 28, 2021
Published: September 21, 2021

REFERENCES

Abhilash, K.P.P., Ahmed, A.S.I., Sathyendra, S., and Abraham, O.C. (2016). Acute pancreatitis due to malaria: A case report of five patients and review of literature. J. Family Med. Prim. Care *5*, 691–694.

Augustin, H.G., and Koh, G.Y. (2017). Organotypic vasculature: From descriptive heterogeneity to functional pathophysiology. Science *357*, eaal2379.

Betts, J.G., Young, K.A., Wise, J.A., Johnson, E., Poe, B., Kruse, D.H., Korol, O., Johnson, J.E., Womble, M., and DeSaix, P. (2013). The Cardiovascular System: Blood Vessels and Circulation. Anatomy and physiology (OpenStax), pp. 887–974. https://openstax.org/books/anatomy-and-physiology/pages/20-1-structure-and-function-of-blood-vessels, Accessed 01 November 2020.

Bowles, L., and Kopelman, P. (2001). Leptin: of mice and men? J. Clin. Pathol. *54*, 1–3.

Boyett, D., and Hsieh, M.H. (2014). Wormholes in host defense: how helminths manipulate host tissues to survive and reproduce. PLoS Pathog. *10*, e1004014.

Cadman, E.T., Abdallah, A.Y., Voisine, C., Sponaas, A.-M., Corran, P., Lamb, T., Brown, D., Ndungu, F., and Langhorne, J. (2008). Alterations of splenic architecture in malaria are induced independently of Toll-like receptors 2, 4, and 9 or MyD88 and may affect antibody affinity. Infect. Immun. *76*, 3924–3931.

Calvo-Alvarez, E., Cren-Travaillé, C., Crouzols, A., and Rotureau, B. (2018). A new chimeric triple reporter fusion protein as a tool for in vitro and in vivo multimodal imaging to monitor the development of African trypanosomes and Leishmania parasites. Infect. Genet. Evol. *63*, 391–403.

Capewell, P., Cren-Travaillé, C., Marchesi, F., Johnston, P., Clucas, C., Benson, R.A., Gorman, T.A., Calvo-Alvarez, E., Crouzols, A., Jouvion, G., et al. (2016). The skin is a significant but overlooked anatomical reservoir for vector-borne African trypanosomes. eLife *5*, e17716.

Carlson, B.E., Arciero, J.C., and Secomb, T.W. (2008). Theoretical model of blood flow autoregulation: roles of myogenic, shear-dependent, and metabolic responses. Am. J. Physiol. Heart Circ. Physiol. *295*, H1572–H1579.

Casas-Sánchez, A., and Acosta-Serrano, Á. (2016). Skin deep. eLife *5*, e21506.

Centers for Disease Control and Prevention (2019). Parasites – African Trypanosomiasis (also known as Sleeping Sickness).. https://www.cdc.gov/parasites/sleepingsickness/biology.html.

Chien, S., Usami, S., Taylor, H.M., Lundberg, J.L., and Gregersen, M.I. (1966). Effects of hematocrit and plasma proteins on human blood rheology at low shear rates. J. Appl. Physiol. *21*, 81–87.

Cook, M.J. (1965). The Anatomy of the Laboratory Mouse (Academic Press). http://www.informatics.jax.org/cookbook/.

Coppola, G., and Caro, C. (2009). Arterial geometry, flow pattern, wall shear and mass transport: potential physiological significance. J. R. Soc. Interface *6*, 519–528.

Corbett, C.E.P., Scremin, L.H.G., Lombardi, R.A., Gama-Rodrigues, J.J., and Okumura, M. (2002). Pancreatic lesions in acute experimental Chagas' disease. Rev. Hosp. Clin. Fac. Med. Sao Paulo *57*, 63–66.

Curtis, A., Calabro, K., Galarneau, J.-R., Bigio, I.J., and Krucker, T. (2011). Temporal variations of skin pigmentation in C57BL/6 mice affect optical bioluminescence quantitation. Mol. Imaging Biol. *13*, 1114–1123.

De Niz, M., Ullrich, A.-K., Heiber, A., Blancke Soares, A., Pick, C., Lyck, R., Keller, D., Kaiser, G., Prado, M., Flemming, S., et al. (2016). The machinery underlying malaria parasite virulence is conserved between rodent and human malaria parasites. Nat. Commun. *7*, 11659.

De Niz, M., Meehan, G.R., and Tavares, J. (2019a). Intravital microscopy: Imaging host-parasite interactions in lymphoid organs. Cell. Microbiol. *21*, e13117.

De Niz, M., Meehan, G.R., Brancucci, N.M.B., Marti, M., Rotureau, B., Figueiredo, L.M., and Frischknecht, F. (2019b). Intravital imaging of host-parasite interactions in skin and adipose tissues. Cell. Microbiol. *21*, e13023.

De Niz, M., Nacer, A., and Frischknecht, F. (2019c). Intravital microscopy: Imaging host-parasite interactions in the brain. Cell. Microbiol. *21*, e13024.

De Niz, M., Carvalho, T., Penha-Gonçalves, C., and Agop-Nersesian, C. (2020). Intravital imaging of host-parasite interactions in organs of the thoracic and abdominopelvic cavities. Cell. Microbiol. *22*, e13201.

Doyle, T.C., Burns, S.M., and Contag, C.H. (2004). In vivo bioluminescence imaging for integrated studies of infection. Cell. Microbiol. *6*, 303–317.

Dufurrena, Q., Amjad, F.M., Scherer, P.E., Weiss, L.M., Nagajyothi, J., Roth, J., Tanowitz, H.B., and Kuliawat, R. (2017). Alterations in pancreatic β cell function and Trypanosoma cruzi infection: evidence from human and animal studies. Parasitol. Res. *116*, 827–838.

Egawa, G., Nakamizo, S., Natsuaki, Y., Doi, H., Miyachi, Y., and Kabashima, K. (2013). Intravital analysis of vascular permeability in mice using two-photon microscopy. Sci. Rep. *3*, 1932.

Engwerda, C.R., Beattie, L., and Amante, F.H. (2005). The importance of the spleen in malaria. Trends Parasitol. *21*, 75–80.

Fernandes, M.C., and Andrews, N.W. (2012). Host cell invasion by Trypanosoma cruzi: a unique strategy that promotes persistence. FEMS Microbiol. Rev. *36*, 734–747.

Fonager, J., Pasini, E.M., Braks, J.A.M., Klop, O., Ramesar, J., Remarque, E.J., Vroegrijk, I.O.C.M., van Duinen, S.G., Thomas, A.W., Khan, S.M., et al. (2012). Reduced CD36-dependent tissue sequestration of Plasmodium-infected erythrocytes is detrimental to malaria parasite growth in vivo. J. Exp. Med. *209*, 93–107.

Franke-Fayard, B., Fonager, J., Braks, A., Khan, S.M., and Janse, C.J. (2010). Sequestration and tissue accumulation of human malaria parasites: can we learn anything from rodent models of malaria? PLoS Pathog. *6*, e1001032.

Glaharn, S., Punsawad, C., Ward, S.A., and Viriyavejakul, P. (2018). Exploring pancreatic pathology in Plasmodium falciparum malaria patients. Sci. Rep. *8*, 10456.

Guérin, A., and Striepen, B. (2020). The Biology of the Intestinal Intracellular Parasite Cryptosporidium. Cell Host Microbe *28*, 509–515.

Hickey, M.J., Kanwar, S., McCafferty, D.-M., Granger, D.N., Eppihimer, M.J., and Kubes, P. (1999). Varying roles of E-selectin and P-selectin in different microvascular beds in response to antigen. J. Immunol. *162*, 1137–1143.

Hopp, C.S., Chiou, K., Ragheb, D.R.T., Salman, A.M., Khan, S.M., Liu, A.J., and Sinnis, P. (2015). Longitudinal analysis of Plasmodium sporozoite motility in the dermis reveals component of blood vessel recognition. eLife *4*, e07789.

Hull, D., and Segall, M.M. (1966). Distinction of brown from white adipose tissue. Nature *212*, 469–472.

Hviid, L., and Jensen, A.T.R. (2015). PfEMP1 – A parasite protein family of key importance in Plasmodium falciparum malaria immunity and pathogenesis. In Advances in Parasitology, D. Rollinson and J.R. Stothard, eds. (Academic Press), pp. 51–84.

Kristensson, K., Nygård, M., Bertini, G., and Bentivoglio, M. (2010). African trypanosome infections of the nervous system: parasite entry and effects on sleep and synaptic functions. Prog. Neurobiol. *91*, 152–171.

Krüger, T., and Engstler, M. (2018). The Fantastic Voyage of the Trypanosome: A Protean Micromachine Perfected during 500 Million Years of Engineering. Micromachines (Basel) *9*, 63.

Lima, T.S., and Lodoen, M.B. (2019). Mechanisms of Human Innate Immune Evasion by *Toxoplasma gondii*. Front. Cell. Infect. Microbiol. *9*, 103.

Magez, S., Pinto Torres, J.E., Obishakin, E., and Radwanska, M. (2020). Infections With Extracellular Trypanosomes Require Control by Efficient Innate Immune Mechanisms and Can Result in the Destruction of the Mammalian Humoral Immune System. Front. Immunol. *11*, 382.

Martello, L.A., Wadgaonkar, R., Gupta, R., Machado, F.S., Walsh, M.G., Mascareno, E., Tanowitz, H.B., and Haseeb, M.A. (2013). Characterization of Trypanosoma cruzi infectivity, proliferation, and cytokine patterns in gut and pancreatic epithelial cells maintained in vitro. Parasitol. Res. *112*, 4177–4183.

Martin-Jaular, L., Ferrer, M., Calvo, M., Rosanas-Urgell, A., Kalko, S., Graewe, S., Soria, G., Cortadellas, N., Ordi, J., Planas, A., et al. (2011). Strain-specific spleen remodelling in Plasmodium yoelii infections in Balb/c mice facilitates adherence and spleen macrophage-clearance escape. Cell. Microbiol. *13*, 109–122.

Muller, W.A. (2002). Leukocyte-endothelial cell interactions in the inflammatory response. Lab. Invest. *82*, 521–533.

Muller, W.A. (2013). Getting leukocytes to the site of inflammation. Vet. Pathol. *50*, 7–22.

Nassief Beshay, E.V., El-Refai, S.A., Helwa, M.A., Atia, A.F., and Dawoud, M.M. (2018). Toxoplasma gondii as a possible causative pathogen of type-1 diabetes mellitus: Evidence from case-control and experimental studies. Exp. Parasitol. *188*, 93–101.

Onyilagha, C., and Uzonna, J.E. (2019). Host Immune Responses and Immune Evasion Strategies in African Trypanosomiasis. Front. Immunol. *10*, 2738.

Oster, C.N., Koontz, L.C., and Wyler, D.J. (1980). Malaria in asplenic mice: effects of splenectomy, congenital asplenia, and splenic reconstitution on the course of infection. Am. J. Trop. Med. Hyg. *29*, 1138–1142.

Prudêncio, M., Rodriguez, A., and Mota, M.M. (2006). The silent path to thousands of merozoites: the Plasmodium liver stage. Nat. Rev. Microbiol. *4*, 849–856.

Rénia, L., and Goh, Y.S. (2016). Malaria Parasites: The Great Escape. Front. Immunol. *7*, 463.

Rosell, M., Kaforou, M., Frontini, A., Okolo, A., Chan, Y.-W., Nikolopoulou, E., Millership, S., Fenech, M.E., MacIntyre, D., Turner, J.O., et al. (2014). Brown and white adipose tissues: intrinsic differences in gene expression and response to cold exposure in mice. Am. J. Physiol. Endocrinol. Metab. *306*, E945–E964.

Saely, C.H., Geiger, K., and Drexel, H. (2012). Brown versus white adipose tissue: a mini-review. Gerontology *58*, 15–23.

Schneider, C.A., Rasband, W.S., and Eliceiri, K.W. (2012). NIH Image to ImageJ: 25 years of image analysis. Nat. Methods *9*, 671–675.

Schnoor, M., Alcaide, P., Voisin, M.-B., and van Buul, J.D. (2015). Crossing the Vascular Wall: Common and Unique Mechanisms Exploited by Different Leukocyte Subsets during Extravasation. Mediators Inflamm. *2015*, 946509.

Secomb, T.W. (2016). Hemodynamics. Compr. Physiol. *6*, 975–1003.

Shi, C., and Liu, E. (2014). Anatomy, histology, and function of the pancreas. In Pathobiology of Human Disease, L.M. McManus and R.N. Mitchell, eds. (Academic Press), pp. 2229–2242.

Silva Pereira, S., Trindade, S., De Niz, M., and Figueiredo, L.M. (2019). Tissue tropism in parasitic diseases. Open Biol. *9*, 190036.

Smith, J.D., Gamain, B., Baruch, D.I., and Kyes, S. (2001). Decoding the language of var genes and Plasmodium falciparum sequestration. Trends Parasitol. *17*, 538–545.

Theron, M., Hesketh, R.L., Subramanian, S., and Rayner, J.C. (2010). An adaptable two-color flow cytometric assay to quantitate the invasion of erythrocytes by Plasmodium falciparum parasites. Cytometry A *77*, 1067–1074.

Trindade, S., Rijo-Ferreira, F., Carvalho, T., Pinto-Neves, D., Guegan, F., Aresta-Branco, F., Bento, F., Young, S.A., Pinto, A., Van Den Abbeele, J., et al. (2016). Trypanosoma brucei Parasites Occupy and Functionally Adapt to the Adipose Tissue in Mice. Cell Host Microbe *19*, 837–848.

Tucker, W.D., Arora, Y.M.K., and Mahajan, K. (2020). Anatomy, Blood Vessels (StatPearls).

Urban, B.C., Hien, T.T., Day, N.P., Phu, N.H., Roberts, R., Pongponratn, E., Jones, M., Mai, N.T.H., Bethell, D., Turner, G.D.H., et al. (2005). Fatal Plasmodium falciparum malaria causes specific patterns of splenic architectural disorganization. Infect. Immun. *73*, 1986–1994.

Venugopal, K., Hentzschel, F., Valkiūnas, G., and Marti, M. (2020). Plasmodium asexual growth and sexual development in the haematopoietic niche of the host. Nat. Rev. Microbiol. *18*, 177–189.

Vestweber, D. (2015). How leukocytes cross the vascular endothelium. Nat. Rev. Immunol. *15*, 692–704.

Wettschureck, N., Strilic, B., and Offermanns, S. (2019). Passing the Vascular Barrier: Endothelial Signaling Processes Controlling Extravasation. Physiol. Rev. *99*, 1467–1525.

Zhang, F., Hao, G., Shao, M., Nham, K., An, Y., Wang, Q., Zhu, Y., Kusminski, C.M., Hassan, G., Gupta, R.K., et al. (2018). An adipose tissue atlas: an image-guided identification of human-like BAT and beige depots in rodents. Cell Metab. *27*, 252–262.e3.

STAR★METHODS

KEY RESOURCES TABLE

REAGENT or RESOURCE	SOURCE	IDENTIFIER
Antibodies		
Alexa Fluor 647 anti-mouse CD36 clone HM36. Isotype Armenian Hamster IgG 0.5mg/ml	BioLegend	Cat# 102610; RRID: AB_528794
Alexa Fluor 647 rat anti-mouse CD62P (P-selectin) clone RB40.34 0.2mg/ml	BD PharMingen	Cat# 563674; RRID: AB_2738366
Alexa Fluor 647 anti-mouse CD102 (ICAM2) clone 3C4 (MIC2/4). Isotype Rat IgG2a,k	BioLegend	Cat# 105612; RRID: AB_2122182
Alexa Fluor 647 anti-mouse CD54 (ICAM1) clone YN1/1.7.4. Isotype Rat IgG2b,k	BioLegend	Cat# 116114; RRID: AB_493495
Alexa Fluor 647 anti-mouse CD31 (PECAM1) clone 390. Isotype Rat IgG2a,k	BioLegend	Cat# 102416; RRID: AB_493410
Mouse CD106/VCAM-1 FITC conjugate	Invitrogen	Cat# RMCD10601; RRID: AB_2556575
Purified Rat Anti-mouse CD102	BD PharMingen	Cat#553326; RRID: AB_394784
Blocking antibody RB40.34 against CD62-P	BD Biosciences	Cat# 553742; RRID: AB_2254315
Blocking antibody P2H3 against CD62-E	eBioscience	Cat# 14-0627-82; RRID: AB_1210768
Blocking antibody CBR 1C2/2 against CD102	eBioscience	Cat# BMS109; RRID: AB_10598677
Blocking antibody YN1/1.7.4 against CD45	eBioscience	Cat#16-0541-85; RRID: AB_468980
Blocking antibody against CD31	abcam	Cat#ab32457; RRID: AB_726369
Blocking antibody against CD36 (185-1G2)	ThermoFisher	Cat# sc-21772; RRID: AB_627042
Blocking antibody Mouse IgG1 K isotype control (P3.6.2.8.1)	eBioscience, ThermoFisher	Cat# 16-4714-82; RRID: AB_470161
Blocking antibody Mouse IgG2 K isotype control (eBM2a)	eBioscience, ThermoFisher	Cat# 14-4724-82; RRID: AB_470114
Bacterial and virus strains		
Viral envelope vector VSVG	Addgene	Plasmid #45494
Chemicals, peptides, and recombinant proteins		
mCD36/Fc chimera (recombinant mouse, CHO cell-derived)	R&D systems	Cat# 2519-CD
Critical commercial assays		
Chemotaxis 24-well cell migration assay kit	Merck	ECM505
Experimental models: Cell lines		
HEK293T	ATCC	CRL3216; RRID: CVCL_0063
HUVECs	Lonza	C2519A
Experimental models: Organisms/strains		
Mouse: C57BL/6	Charles River	Strain code: 027
Mouse: C57BL/6 Albino	Charles River	Strain code: 493
Mouse: CD36−/−	Jackson laboratories	Stock code: 019006
Mouse: CD36+/+	In house breeding	
Mouse: CD36+/−	In house breeding	
Oligonucleotides		
pLenti-C-mGFT-P2A-Puro	OriGENE	PS100093
Cd36 (NM_007643) Mouse Tagged ORF Clone Lentiviral Particle	OriGENE	MR227663L4

(*Continued on next page*)

Continued

REAGENT or RESOURCE	SOURCE	IDENTIFIER
Software and algorithms		
ImageJ	(Schneider et al., 2012)	https://imagej.nih.gov/ij/

RESOURCE AVAILABILITY

Lead contact

Further information and requests for resources and reagents should be directed to and will be fulfilled by the lead contact, Luisa Miranda Figueiredo (lmf@medicina.ulisboa.pt).

Materials availability

This study did not generate new unique reagents.

Data and code availability

- All data used for the generation of figures in this paper has been included in Data S1.
- This paper does not report original code.
- Any additional information required to reanalyze the data reported in this paper is available from the lead contact upon request.

EXPERIMENTAL MODEL AND SUBJECT DETAILS

Animals used

Animal experiments were performed according to EU regulations and approved by the Animal Ethics Committee of Instituto de Medicina Molecular (IMM) (AEC_2011_006_LF_TBrucei_IMM). Mice used across this study included wild-type male C57BL/6J mice, and C57BL/6 Albino obtained from Charles River, France. Transgenic B6.129S1-Cd36^{tm1Mfe}/J (CD36$^{-/-}$) mice were obtained from The Jackson Laboratory. Breedings were generated in-house at IMM. A homozygous KO line was kept over multiple generations. A heterozygous (CD36$^{+/-}$) line was generated by crossing CD36$^{-/-}$ mice with C57BL/6J mice, and a homozygous CD36$^{+/+}$ line was generated through backcrossing. Mice were backcrossed over multiple generations, and littermates of all 3 genotypes were used throughout this work. All mice were 6–9 weeks old males, with an average weight ranging between 25 and 30 g.

Trypanosoma brucei parasites and infections

Mice were infected by intraperitoneal injection of 2,000 T. brucei AnTat 1.1^{E} chimeric triple reporter parasites (Calvo-Alvarez et al., 2018) expressing the red-shifted firefly luciferase protein PpyREH9, TdTomato and ty1. For parasite counts, blood samples were taken daily by tail vein puncture, using 1μl of blood diluted in 200 μl of HMI11 medium, and 10 μm loaded in a hemocytometer for parasite quantification. For mouse survival, mice were followed up until clinical signs indicating no recovery. After determining the time of highest disease recrudescence in the survival experiments, all other experiments were capped to 20 days of infection.

HUVECs cell culture

Human umbilical vein ECs (HUVECs – Lonza, C2519A) were routinely cultured following the manufacturer's guidelines at 37°C and 5% of CO_2 with complete medium EGM-2 Bulletkit (Lonza, CC-3162) without antibiotics. All the experiments were performed between passages 2 and 4.

When passaging HUVECs for experiments, cells were washed twice in sterile PBS (137mM NaCl, 2.7mM KCl, 4.3mM Na2HPO4, 1.47mM KH2PO4, pH7.4) and then incubated for 5min in TrypLE Express Enzyme (1X) (Alfagene, 12605028) at 37°C, 5% CO2. When 95% of the cells detached, complete medium was added to each flask to inhibit the activity of the TrypLE Express Enzyme and the cell suspension was transferred into a falcon tube. Cells were then centrifuged at 700rpm for 5min at 10°C and the pellet re-suspended in fresh complete medium. HUVECs were then seeded at the desired concentration, depending on the experiments.

HUVECs viral transduction

Replication-incompetent lentiviruses were produced by transient transfection of HEK293T co-transfected with the viral packaging vector Δ8.9 and the viral envelope vector VSVG. Medium was replaced with fresh culture medium 4-6h post transfection. 48h after post transfection, lentiviral particles were concentrated from supernatant by ultracentrifugation at 90000 g for 1h30 and re-suspended in 0.1% BSA PBS. HUVECs were transduced 24h after seeding with 1% lentiviral plasmids containing GFP (control) (pLenti-C-mGFT-P2A-Puro, Cat # PS100093, Origene) or CD36-GFP (NM_007643, Cat # MR227663L4, Origene) sequences. 24h

after viral transduction, media was replaced by fresh complete medium. Cells were then kept in culture until 48h post-transduction and then processed for *T. brucei* co-culture and imaging.

METHOD DETAILS

Bioluminescence imaging (*in vivo* and *ex vivo*)

For whole body imaging, infected mice were injected with 200 μl of RediJect D-luciferin (Xenolight, Perkin Elmer) prior to imaging. All measurements were performed in an IVIS Lumina imaging system. A kinetic curve was established to determine the peak of bioluminescence, which was found to be at 10 minutes post-injection, with a plateau lasting a further 10 minutes. For *in vivo* imaging, mice were anaesthetized with Isofluorane (Isotroy) and imaged using an exposure time of 1 minute and a FOV D (12.5 × 12.5 cm). For *ex vivo* imaging of non-perfused organs, mice were injected with RediJect as described above, and sacrificed using CO_2 within 3 minutes following this injection. Organs were then extracted, washed in 1x PBS, and placed in a plastic Petri dish for imaging at the IVIS Lumina instrument, using an exposure time of 1 minute and a FOV C (10 × 10 cm). For *ex vivo* imaging of perfused organs, mice were injected with RediJect as described above, and sacrificed using CO_2 within 3 minutes following this injection. The chest was then exposed, the inferior vena cava was cut, and the heart was injected with 40 mL of warm 1x PBS. Organs were then imaged as described above. Image acquisition was obtained, and image analysis performed using the Living Image ® software version 3.0.4.6. For all bioluminescence measures, the results of 9 animals (3 biological replicates in triplicate) are expressed.

Intravital and *ex vivo* imaging

For intravital imaging, surgeries were separately performed in the brain; the lungs and heart; the liver; the pancreas, spleen and kidney; the adipose tissues and lymph nodes, as described in De Niz et al. (2019a, 2019b, 2019c, 2020). Briefly, mice were anaesthetized with a mixture of ketamine (120 mg/kg) and xylazine (16 mg/kg) injected intraperitonially. After checking for reflex responses and ensuring none occurred, mice were intraocularly injected with Hoechst 33342 (stock diluted in dH_2O at 100 mg/ml; injection of 40 μg/kg mouse), 70 kDa FITC-Dextran (stock diluted in 1x PBS at stock concentration of 100 mg/ml; injection of 500 mg/kg), and vascular markers of interest conjugated to A647 (CD31 (Biolegend, used at 20 μg), Ephrin B2 (R&D systems, used at 20 μg), Eph-B4 (R&D systems, used at 20 μg), or VEGFR3 (R&D systems, used at 20 μg). A temporary glass window (Merk rectangular coverglass, 100 mm x 60 mm or circular coverglass (12 mm)) was implanted in each organ, and secured either surgically, with surgical glue, or via a vacuum, in order to enable visualization of the organ surface.

For intravital microscopy, all imaging relative to parasite quantifications, vascular density and vascular leakage was done in a Zeiss Cell Observer SD (spinning disc) confocal microscope (Carl Zeiss Microimaging, equipped with a Yokogawa CSU-X1 confocal scanner, an Evolve 512 EMCCD camera and a Hamamatsu ORCA-flash 4.0 VS camera) or in a 3i Marianas SDC (spinning disc confocal) microscopy (Intelligent Imaging Innovations, equipped with a Yokogawa CSU-X1 confocal scanner and a Photometrics Evolve 512 EMCCD camera). Laser units 405, 488, 561 and 640 were used to image Hoechst in nuclei, extravascular and intravascular FITC-Dextran, TdTomato in *T. brucei,* and CD31, respectively. The objective used to image vascular density, vascular leakage, and proportion of intravascular and extravascular parasites was a 40x LD C-Apochoromat corrected, water immersion objective with 1.1 NA and 0.62 WD. The objective used to classify *T. brucei* movement phenotypes was a 100x plan-apochromat, oil immersion objective with 1.4 NA and 0.17 WD. Between 20 and 100 images were obtained in any one time lapse, with an acquisition rate of 20 frames per second. For vascular density measurements and parasite quantification, in order to gain access to the full organ, we performed *ex vivo* imaging from different organ regions. For this, we performed z stacks consisting of 16 stacks covering up to 200 μm of tissue depth. For all acquisitions, the software used was ZEN blue edition v.2.6 (for the Zeiss Cell Observed SD) allowing export of images in .czi format, and 3i Slidebook reader v.6.0.22 (for the 3i Marianas SD), allowing export of images in TIFF format.

Intravascular and extravascular parasite quantification

In order to quantify intravascular and extravascular parasites, we took as reference, the vascular marker CD31-A647 and 70 kDa FITC-Dextran, and we quantified numbers of *T. brucei* parasites within the confines of the regions marked by the vascular marker, and numbers of parasites outside these regions. We then normalized the total quantity to numbers per mm^2 so as to be able to compare both measurements. Measurements were repeated throughout 20 days of infection, and at least a total of 100 fields of view were quantified.

Vascular density and diameter quantification

In order to quantify vascular density, we took as reference the vascular marker CD31-A647 and 70 kDa FITC-Dextran. We obtained 100 fields of view, and for each field of view the total area was defined as 100%. Using the CD31 signal we were able to segment out the vascular regions using Fiji software. We calculated the percentage of vascular area covered using the following formula: $A_{V\%} = \frac{A_V \times A_{T\%}}{A_T}$, where A_T is the total area of the field of view, $A_{T\%}$ is 100, and A_{TV} is the total area marked by CD31. Vascular density measurements were performed throughout 20 days of infection. Vessel diameters were measured using Fiji.

Vascular permeability quantification

In order to quantify vascular permeability changes, we took as reference the marker 70 kDa FITC-Dextran as previously published methodology (Egawa et al., 2013). We measured FITC-Dextran in intravascular and extravascular regions in uninfected mice, and then at each time post-infection with *T. brucei.* The permeability ratio was calculated using the following equation: $Permeability\ Ratio_{D_n} = \frac{Mean\ MFI_{D_n}}{Mean\ MFI\ D_0}$, where mean MFI_{Dn} is the extravascular MFI at a specific Day *n*, and the mean MFI_{D0} is the extravascular MFI in uninfected mice (Day 0). To induce vascular hyper-permeability, 5 mg/ml of histamine (Sigma-Aldrich) were prepared in 1 x PBS, and 200 μl were injected intravenously every 2 days, starting 2 days prior to infection.

Erythrocyte labeling and parasite quantification normalization by vascular type

To quantify and normalize parasite numbers per vascular type, red blood cells were extracted from uninfected mice, and pre-labeled ex-vivo with intracellular dyes CFDA-SE or DDAO-SE as previously described (Theron et al., 2010). The required volume of erythrocytes at 5% hematocrit were resuspended in 500 μl HMI11. RBCs were centrifuged and the pellet resuspended either in 20 μM carboxfluorescein diacetate succinimidyl ester (CFDA-SE) (Invitrogen), or 10 μM 7-hydroxy-9H-(1,3-dichloro-9,9-dimethylacridin-2-one) succinimidyl ester (DDAO-SE) (Invitrogen) in HMI11 and incubated for 20 min at 37°C. The suspension was washed 3x in HMI11, and resuspended at concentrations equaling those observed for parasites at each day post-infection. The labeled RBCs were then injected into infected mice. The number of RBCs per vessel type were quantified, and the number of parasites expressed as a percentage of labeled RBCs in any one vessel as follows:

$$Relativeparasite\ \%\ D_n = \frac{ParasitenumbersD_n \times labeledRBC_{T\%}}{labeledRBCnumbersD_n}$$

The value of *Relative parasite* % at Day *n* (D_n) was plotted and color coded in heatmaps based on total vasculature, arterial vasculature, or venous vasculature.

Labeling endothelial receptors

To investigate the relative expression of EC receptors in different organs, we intravenously injected 20 μg of antibodies against E-selectin, P-selectin (BD PharMingen), ICAM1, ICAM2, PECAM1, CD36 (BioLegend) and VCAM1 (Invitrogen) conjugated to FITC (VCAM1) or A647 (all other antibodies), into uninfected or day 6 infected mice, as previously described in the context of parasitology for CD31 (Hopp et al., 2015). We measured MFIs of at least 100 different vessels per organ in 3 separate mice using an LSM 710 Zeiss microscope, a 40x objective (1.3 NA).

Blocking endothelial receptors

To investigate the effects of blocking various EC receptors, antibodies used included RB40.34 against P-selectin (BD Biosciences, 30 μg per mouse); P2H3 against E-selectin (R&D systems, 20 μg per mouse), a 1:1 combination of both; CBR IC2/2 against ICAM2 (Invitrogen, 20 μg per mouse); YN1/1.7.4 against ICAM1 (eBioscience, 20 μg per mouse); CD31 antibody (abcam, 20 μg per mouse); and 185-1G2 against CD36 (Abcam, 20 μg per mouse) blocking antibodies were used. Mouse IgG1 and IgG2 isotype controls were used as controls (eBioscience). Antibodies were injected intravenously daily by tail vein injection, starting two days prior to infection, and continuing until day 6 post-infection.

Recombinant CD36 binding assays

For *in vitro* measurement of *T. brucei* attachment to CD36, we coated dishes with recombinant mouse CD36/Fc chimera (R&D). Triplicate plastic dishes were prepared for each concentration. They were first washed with 1x PBS, and then blocked with 1% (wt/v) bovine serum albumin (BSA) at 4°C overnight. After washing once with 1x PBS, dishes were coated with recombinant mouse CD36 (2nM, 5nM, 10nM, 50nM, 100nM and 200nM), or with 1x PBS (control 1) or 1x PBS containing 1% BSA (cell culture grade; control 2) for 3h at 37°C in a cell culture incubator. Following this time, plates were washed 3 times and incubated again with 1% BSA in PBS for 30 minutes. One million *T. brucei* in HMI-11 were overlayed on the dishes for 1h. After 1h, total parasites were quantified by microscopy prior to performing washouts with fresh HM1-11 media. After washouts, bound parasites were quantified by microscopy. Each condition was done in triplicate and each experiment repeated 3 times.

CD36 binding assays in HUVECs

T. brucei parasites were diluted to a concentration of 0.5 million parasites per ml, and 1ml was overlayed on wells in 24-well plates containing control and CD36-expressing HUVECs for 0.5, 1, 2, 4, 6 and 8 hours. Separate wells were used for each time point. At each time point, total parasites were quantified by microscopy prior to performing washouts. After washouts to remove any unbound parasites, attached parasites were quantified by microscopy.

CD36 transmigration assays in HUVECs

For transmigration assays, a QCM chemotaxis cell migration assay (24 well-plates, 3 μm) (MERCK, ECM 504) was used. WT, GFP- and CD36-expressing HUVECs were seeded in the base of the upper chamber of the transwell set, in complete medium. The lower chamber was also filled with complete medium. Half a million *T. brucei* parasites suspended in 250 μl of HMI-11 were over-

layed on the ECs in the upper chamber, and the co-culture was maintained for 1 hour. At time point zero, parasites were quantified in the upper and lower chambers by microscopy. At 1h post-co-culture, parasites in the upper and lower chambers were again quantified.

QUANTIFICATION AND STATISTICAL ANALYSIS

Data were displayed in graphs and heatmaps generated using Prism 9 software (GraphPad). Means, medians, survival, correlation tests, comparison tests, and error measures were calculated from triplicate experiments with 3 biological replicates each, and/or at least 100 images per condition. For comparisons of bioluminescence measures between organs of different groups we performed multiple t tests in addition to a one-way ANOVA (differences were considered significant when $p < 0.05$). Pearson correlations measures (R), and R^2 values were calculated to determine the strength of linear association between parasite density and either vascular permeability or vascular density. For comparison of proportions between parasites in vessels of different diameters and proportions in vessels of equal diameter across vascular groups, a linear model was performed, and p values < 0.05 were considered significant. For comparisons of survival, a log-rank (Mantel-Cox) test was performed, and p values < 0.05 were considered significant. Statistical details of experiments are included in the figure legends, the results section, and a Supplementary Table excel file. All data used for the generation of the figures is included as a supporting file.